

A multi-resolution SPH method for fluid-structure interactions

Chi Zhang, Massoud Rezavand, Xiangyu Hu *



Department of Mechanical Engineering, Technical University of Munich, 85748 Garching, Germany

ARTICLE INFO

Article history:

Received 14 December 2019

Received in revised form 14 October 2020

Accepted 22 November 2020

Available online 8 December 2020

Keywords:

Fluid-elastic structure interaction

Multiple time steps

Multi-resolution

Smoothed particle hydrodynamics

ABSTRACT

In this paper, we present a multi-resolution smoothed particle hydrodynamics (SPH) method for modeling fluid-structure interaction (FSI) problems. By introducing different smoothing lengths and time steps, the spatial-temporal discretization is applied with different resolutions for fluid and structure. To ensure momentum conservation at the fluid-structure coupling, a position-based Verlet time integration scheme is introduced. Furthermore, the time-averaged velocity and acceleration of solid particles are introduced to enhance force matching in the fluid and solid equations. A set of numerical examples including several bio-mechanical problems are considered to demonstrate the efficiency, accuracy and robustness of the present method. An open-source code for all the examples is also provided.

© 2020 Elsevier Inc. All rights reserved.

1. Introduction

Fluid-structure interaction (FSI) problems, in particular those involving flexible and deformable elastic structures, are ubiquitous in natural phenomena, e.g. aerial animal flying and aquatic animal swimming, and play a key role in a vast range of engineering examples, e.g. hydroelastic slamming, energy harvesting and prosthetic heart valves. Due to the intrinsic complexity of the surrounding flow and the large deformation of the structure, computational study of FSI problems is highly challenging.

Mesh-based approaches, such as the finite element method (FEM) [1] and immersed-boundary method (IBM) [2], can encounter difficulties for simulating FSI problems. Typical difficulties for FEM include the treatment of the convective terms and the updating of the meshes for moving fluid-structure interface, especially when large structure deformation is taken into account [3]. IBM utilizes two overlapped Lagrangian and Eulerian meshes. While the fluid equation is solved on the Eulerian mesh, the effects of solid structure are taken into account by distributing the forces computed on the deformed Lagrangian mesh to the Eulerian mesh using a kernel function. Such fairly weak coupling formulation leads to the Lagrangian-Eulerian mismatches on the kinematics and the distribution of solid structure forces.

An alternative approach for tackling FSI problems is to discretize both the fluid and solid equations by using Lagrangian meshfree methods, for instance smoothed particle hydrodynamics (SPH) [4–6], the moving-particle semi-implicit method (MPS) [7] and discrete element method (DEM) [8]. Owing to their peculiar advantages in handling material interfaces [9,10], and the capability of capturing violent events such as wave impact and breaking [11], Lagrangian particle-based methods can be conspicuously effective when studying FSI problems, in particular, when they are characterized by large displacement of fluid-structure interfaces. Promising results have been obtained by the weakly-compressible SPH method [12–19,11].

* Corresponding author.

E-mail addresses: c.zhang@tum.de (C. Zhang), massoud.rezavand@tum.de (M. Rezavand), xiangyu.hu@tum.de (X. Hu).

incompressible SPH method [20–22], MPS method [23] and SPH-DEM method [24], and also their combinations with FEM [25–27]. It is worth to note that Khayyer et al. proposed the first multi-resolution FSI solver based on MPS method [23].

When the SPH method is used for studying FSI problems, single spatial-temporal resolution is commonly employed for the discretization of fluid and solid equations [12]. Specifically, a uniform particle spacing is used for the entire computational domain and a single time step, which is the smallest of these required by the fluid and solid structure [12], is applied for time integration. From the computational efficiency point of view, the single-resolution approach can be rather expensive in applications where the structure requires locally refined resolution. This is the case when the structure is relatively thin, i.e. the structure has a considerable small spatial scale compared with fluid. This is also the case when the structure has a high Poisson ratio which results smaller time step size than that required by the fluid. Therefore, developing a multi-resolution SPH method capable of employing various resolutions for fluid and solid structure is desirable.

In this paper, we propose a multi-resolution SPH method to increase the computational efficiency for simulating FSI problems. Following the unified SPH discretization in Ref. [17], the update Lagrangian formulation is utilized for the fluid dynamics, and the total Lagrangian formulation for solid dynamics. Since the solid structure is able to be resolved at a higher spatial resolution, the computational efficiency is enhanced when a lower resolution discretization for the fluid is sufficient. To further improve the efficiency, different time steps are employed for integrating the fluid and solid equations. A position-based Verlet time integration scheme is proposed for enforcing the momentum conservation at the fluid-structure coupling. The velocity and acceleration of solid particles are averaged over a fluid time step to enhance the force matching, e.g. calculates a set of reliable interaction forces over a single fluid time step during which structure state has been updated several times, in fluid and solid equations. Different from previous researches which attempted to apply different resolutions for the discretization of fluid equations [28–34], the objective of present method is to develop a multi-resolution SPH method for FSI problems. The efficiency, accuracy and robustness of the present method are validated with three benchmark tests, viz. hydrostatic water column on an elastic plate, flow-induced vibration and dam-break flow with elastic gate. Then, two bio-mechanical applications, namely, venous valve and passive flapping of a fish-like body in flow, are considered to demonstrate the versatility and potential of the present method in simulating bio-mechanical systems. The remainder of this paper is arranged as follows: Section 2 briefly summarize the governing equations and preliminary SPH algorithm for simulating FSI problems. The multi-resolution method is detailed in Section 3. Numerical validations and applications are presented and discussed in Section 4. Concluding remarks are given in Section 5 and all the codes and data-sets accompanying this work are available in our open-source library SPHinXsys [35] on GitHub at <https://github.com/Xiangyu-Hu/SPHinXsys>.

2. Governing equations and preliminary work

Before moving to detailed description of the multi-resolution method, we first introduce the governing equations for fluid and solid dynamics, and then briefly summarize the corresponding discretizations with unified SPH formulation and more details are referred to Han and Hu [17].

2.1. Fluid- and solid-dynamics equations

The governing equations in updated Lagrangian formulation for an isothermal and Newtonian fluid flow are the mass conservation equation

$$\frac{d\rho}{dt} = -\rho \nabla \cdot \mathbf{v}, \quad (1)$$

and the momentum conservation equation

$$\rho \frac{d\mathbf{v}}{dt} = -\nabla p + \eta \nabla^2 \mathbf{v} + \mathbf{g}, \quad (2)$$

where ρ is the density, t the time, \mathbf{v} the velocity, p the pressure, η the dynamics viscosity and \mathbf{g} the body force. To close the system of Eqs. (1) and (2), an appropriate equation of state (EoS) for the fluid is required. Following the weakly-compressible model for incompressible flow [36,37], the pressure is evaluated from the density through the Tait equation

$$p = \frac{\rho^0(c^F)^2}{\gamma} \left(\left(\frac{\rho}{\rho^0} \right)^\gamma - 1 \right), \quad (3)$$

where $\gamma = 7$ and the reference density ρ^0 . Here, c^F is the artificial sound speed of fluid. Numerical experiments confirm that the density variations are limited to about 1% [37] when $c^F = 10v_{max}$ with v_{max} denoting the maximum anticipated flow speed.

For the solid structure, an elastic and weakly-compressible material is taken into account. Following the convention in continuum mechanics, the initial position \mathbf{r}^0 of a material point is defined in the initial reference configuration, and the current position \mathbf{r} in the deformed current configuration. Then the displacement \mathbf{u} of a material point, which is obtained by the difference between its current position and initial reference position, can be obtained as

$$\mathbf{u} = \mathbf{r} - \mathbf{r}^0. \quad (4)$$

Thus, the deformation tensor, is defined by

$$\mathbb{F} = \nabla^0 \mathbf{u} + \mathbb{I}, \quad (5)$$

where \mathbb{I} denotes the identity matrix, and $\nabla^0 \equiv \frac{\partial}{\partial \mathbf{r}^0}$ stands for the gradient operator with respect to the initial reference configuration. In the total Lagrangian formulation, the mass conservation equation is given by

$$\rho - \rho^0 J^{-1} = 0, \quad (6)$$

where ρ^0 is the initial reference density and $J = \det(\mathbb{F})$ the Jacobian determinant of deformation tensor \mathbb{F} . The momentum conservation equation reads

$$\rho^0 \frac{d\mathbf{v}}{dt} = \nabla^0 \cdot \mathbb{P}^T, \quad (7)$$

where \mathbb{P}^T is the nominal stress tensor. Here T denotes transpose operation and \mathbb{P} is the 1st Piola-Kirchhoff stress tensor which relates the forces in the current configuration to the areas in the initial reference configuration. For an ideal elastic or Kirchhoff material, \mathbb{P} is given by

$$\mathbb{P} = \mathbb{F} \mathbb{S}, \quad (8)$$

where \mathbb{S} represents the second Piola-Kirchhoff stress which is evaluated via the constitutive equation relating \mathbb{F} with the Green-Lagrangian strain tensor \mathbb{E} defined as

$$\mathbb{E} = \frac{1}{2} (\mathbb{F}^T \mathbb{F} - \mathbb{I}). \quad (9)$$

In particular, when the material is linear elastic and isotropic, the constitutive equation is simply given by

$$\begin{aligned} \mathbb{S} &= K \text{tr}(\mathbb{E}) \mathbb{I} + 2G \left(\mathbb{E} - \frac{1}{3} \text{tr}(\mathbb{E}) \mathbb{I} \right) \\ &= \lambda \text{tr}(\mathbb{E}) \mathbb{I} + 2\mu \mathbb{E}, \end{aligned} \quad (10)$$

where λ and μ are Lamé parameters, $K = \lambda + (2\mu/3)$ the bulk modulus and $G = \mu$ the shear modulus. The relation between the two modulus is given by

$$E = 2G(1 + 2\nu) = 3K(1 - 2\nu) \quad (11)$$

with E denotes the Young's modulus and ν the Poisson ratio. Note that the sound speed of solid structure is defined as $c^S = \sqrt{K/\rho}$. In present work, a Neo-Hookean model defined by the strain-energy density function [38]

$$W = \mu \text{tr}(\mathbb{E}) - \mu \ln J + \frac{\lambda}{2} (\ln J)^2 \quad (12)$$

is used for predicting the nonlinear stress-strain behavior of materials undergoing large deformations. Note that the second Piola-Kirchhoff stress \mathbb{S} can be derived as

$$\mathbb{S} = \frac{\partial W}{\partial \mathbb{E}} \quad (13)$$

from strain-energy density function.

2.2. Preliminary work

A SPH discretization of the mass and momentum conservation equations, Eqs. (1) and (2), can be respectively derived as

$$\frac{d\rho_i}{dt} = 2\rho_i \sum_j V_j (\mathbf{v}_i - \tilde{\mathbf{v}}_{ij}) \nabla_i W_{ij}, \quad (14)$$

and

$$m_i \frac{d\mathbf{v}_i}{dt} = -2 \sum_j V_i V_j \tilde{p}_{ij} \nabla_i W_{ij} + 2 \sum_j \eta V_i V_j \frac{\mathbf{v}_{ij}}{r_{ij}} \frac{\partial W_{ij}}{\partial r_{ij}} + \mathbf{g} + \mathbf{f}_i^{S:p} + \mathbf{f}_i^{S:v}, \quad (15)$$

where V_i denotes the particle volume and $\nabla_i W_{ij} = \nabla_i W(\mathbf{r}_{ij}, h) = \frac{\mathbf{e}_{ij}}{r_{ij}} \frac{\partial W_{ij}}{\partial r_{ij}}$, where $\mathbf{r}_{ij} = \mathbf{r}_i - \mathbf{r}_j$ and h is smoothing length, the unit vector $\mathbf{e}_{ij} = \frac{\mathbf{r}_{ij}}{r_{ij}}$, representing the derivative of the kernel function with respect to \mathbf{r}_i , the position of particle i . Here, the

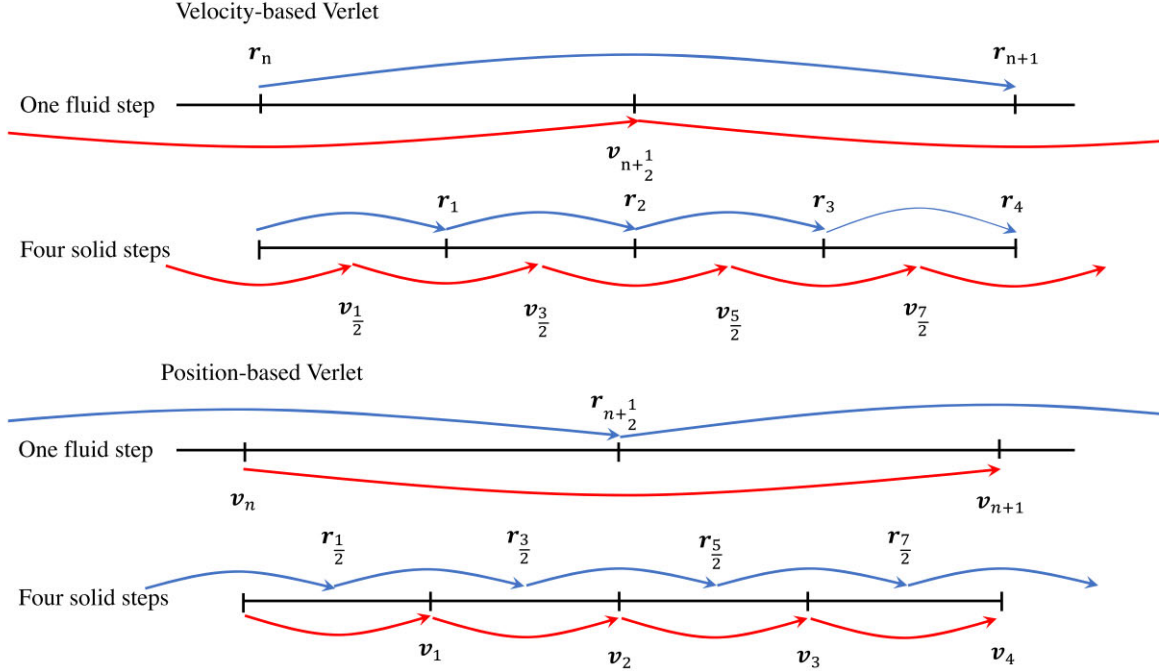


Fig. 1. Sketch of velocity- and position-based Verlet schemes with assumption that $\kappa = 4$.

inter-particle velocity and pressure averages, $\tilde{\mathbf{v}}_{ij}$ and \tilde{p}_{ij} , can be obtained by a simple average, or from the solution of the inter-particle Riemann problem. In the present work, a low-dissipation Riemann solver is applied and we refer to Ref. [6,10] for more details. The $\mathbf{f}_i^{S:p}$ and $\mathbf{f}_i^{S:v}$ terms are the pressure and viscous forces acting on the fluid particle, respectively, due to the presence of the solid structure.

To discretize the governing equations of solid dynamics, a correction matrix \mathbb{B}^0 [39,17] is first introduced to reproducing rigid-body rotation as

$$\mathbb{B}_a^0 = \left(\sum_b V_b^0 (\mathbf{r}_b^0 - \mathbf{r}_a^0) \otimes \nabla_a^0 W_{ab} \right)^{-1}, \quad (16)$$

where

$$\nabla_a^0 W_a = \frac{\partial W(|\mathbf{r}_{ab}^0|, h)}{\partial |\mathbf{r}_{ab}^0|} \mathbf{e}_{ab}^0 \quad (17)$$

stands for the gradient of the kernel function evaluated at the initial reference configuration. Note that subscripts a and b are used to denote solid particles, and smoothing length h is identical to that in the discretization of fluid equations of Eq. (15). Using the initial configuration as the reference, the solid density is directly evaluated as

$$\rho_a = \rho_a^0 \frac{1}{J} \quad (18)$$

from Eq. (6). We can now discretize Eq. (7) in the following form

$$m_a \frac{d\mathbf{v}}{dt} = 2 \sum_b V_a V_b \tilde{\mathbb{P}}_{ab} \nabla_a^0 W_{ab} + \mathbf{g} + \mathbf{f}_a^{F:p} + \mathbf{f}_a^{F:v}, \quad (19)$$

where inter-particle averaged first Piola-Kirchhoff stress $\tilde{\mathbb{P}}$ is defined as

$$\tilde{\mathbb{P}}_{ab} = \frac{1}{2} \left(\mathbb{P}_a \mathbb{B}_a^0 + \mathbb{P}_b \mathbb{B}_b^0 \right). \quad (20)$$

Also $\mathbf{f}_a^{F:p}$ and $\mathbf{f}_a^{F:v}$ correspond to the fluid pressure and viscous forces acting on the solid particle a , respectively.

In fluid-structure coupling, the surrounding solid structure is behaving as a moving boundary for fluid, and the no-slip boundary condition is imposed at the fluid-structure interface. Following Han and Hu [17] and Adami et al. [40], the interaction forces $\mathbf{f}_i^{S:p}$ and $\mathbf{f}_i^{S:v}$ acting on a fluid particle i , due to the presence of the neighboring solid particle a , can be obtained as

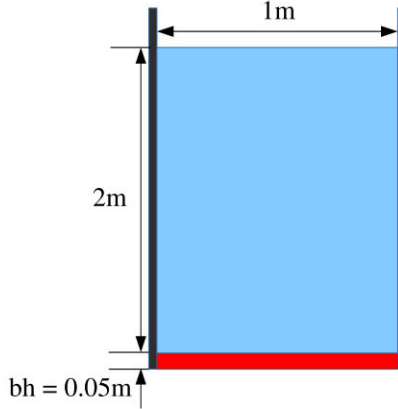


Fig. 2. Schematic sketch of hydrostatic water column on an elastic plate.

Table 1
Hydrostatic water column on an elastic plate: the setup of four different cases.

Cases	dp^F/dp^S	dp^S	Time steps	Number of particles
I	1.0	$dp^S = bh/8.0$	Multiple	51199
II	2.0	$dp^S = bh/8.0$	Multiple	12799
III	4.0	$dp^S = bh/8.0$	Multiple	3199
IV	4.0	$dp^S = bh/8.0$	Single	3199

$$\mathbf{f}_i^{S:p} = -2 \sum_a V_i V_a \frac{p_i \rho_a^d + p_a^d \rho_i}{\rho_i + \rho_a^d} \nabla_i W(\mathbf{r}_{ia}, h), \quad (21)$$

and

$$\mathbf{f}_i^{S:v} = 2 \sum_a \eta V_i V_a \frac{\mathbf{v}_i - \mathbf{v}_a^d}{r_{ia}} \frac{\partial W(\mathbf{r}_{ia}, h)}{\partial r_{ia}}. \quad (22)$$

Here, the imaginary pressure p_a^d and velocity \mathbf{v}_a^d are defined by

$$\begin{cases} p_a^d = p_i + \rho_i \max(0, (\mathbf{g} - \frac{d\mathbf{v}_a}{dt}) \cdot \mathbf{n}^S) (\mathbf{r}_{ia} \cdot \mathbf{n}^S) \\ \mathbf{v}_a^d = 2\mathbf{v}_i - \mathbf{v}_a \end{cases}, \quad (23)$$

where \mathbf{n}^S denotes the surface normal direction of the solid structure, and the imaginary particle density ρ_a^d is calculated through the EoS presented in Eq. (3) [40]. Accordingly, the interaction forces $\mathbf{f}_a^{F:p}$ and $\mathbf{f}_a^{F:v}$ acting on a solid particle a are given by

$$\mathbf{f}_a^{F:p} = -2 \sum_i V_a V_i \frac{p_a^d \rho_i + p_i \rho_a^d}{\rho_i + \rho_a^d} \nabla_a W(\mathbf{r}_{ai}, h), \quad (24)$$

and

$$\mathbf{f}_a^{F:v} = 2 \sum_i \eta V_a V_i \frac{\mathbf{v}_a^d - \mathbf{v}_i}{r_{ia}} \frac{\partial W(\mathbf{r}_{ia}, h)}{\partial r_{ai}}. \quad (25)$$

The anti-symmetric property of the derivative of the kernel function will ensure the momentum conservation for each pair of interacting particles i and a . For time integration, a single time step [12]

$$\Delta t = \min \left[0.25 \min \left(\frac{h}{c^F + |\mathbf{v}|_{max}}, \frac{h^2}{\eta} \right), 0.6 \min \left(\frac{h}{c^S + |\mathbf{v}|_{max}}, \sqrt{\frac{h}{|\frac{d\mathbf{v}}{dt}|_{max}}} \right) \right] \quad (26)$$

is commonly used to ensure momentum conservation and force-calculation matching of fluid-structure interaction. Note that, this may lead to low computational efficiency as a very small time step can be chosen when the sound speed of the solid structure is significantly larger than that of the fluid.

Table 2

Hydrostatic water column on an elastic plate: computational efficiency. The computations are carried out on an Intel(R) Xeon(R) L5520 2.27 GHz desktop computer with 24GiB RAM and a Scientific Linux operating system (6.9). To analyze the computational performance, we evaluate the CPU wall-clock time for shared memory parallelized computations (based on the Intel TBB library) until the 0.1s time instant.

Cases	I	II	III	IV
CPU time (s)	124.41	56.28	40.02	329.48

3. Multi-resolution method

In this section, we present a multi-resolution SPH method, where the fluid and solid equations are discretized by different spatial-temporal resolutions, to increase the computational efficiency. For this, different particle spacing, hence different smoothing lengths, and different time steps are utilized to discretize the fluid and solid equations. Note that, introducing different time steps may result in the issues of momentum conservation and force mismatch in fluid-structure coupling. To address these issues, we propose a position-based Verlet time integration scheme and introduce the time-averaged velocity and acceleration of solid particles for the calculation of interaction forces.

3.1. Multi-resolution discretization

As different spatial resolutions are applied, the fluid discretizations of Eqs. (1) and (2) are modified as

$$\frac{d\rho_i}{dt} = 2\rho_i \sum_j V_j (\mathbf{v}_i - \tilde{\mathbf{v}}_{ij}) \nabla_i W_{ij}^{h^F}, \quad (27)$$

and

$$m_i \frac{d\mathbf{v}_i}{dt} = -2 \sum_j V_i V_j \tilde{p}_{ij} \nabla_i W_{ij}^{h^F} + 2 \sum_j \eta V_i V_j \frac{\mathbf{v}_{ij}}{r_{ij}} \frac{\partial W_{ij}^{h^F}}{\partial r_{ij}} + \mathbf{g} + \mathbf{f}_i^{S:p}(h^F) + \mathbf{f}_i^{S:v}(h^F), \quad (28)$$

where h^F represents the smoothing length used for fluid.

Also, the discretization of solid momentum equation of Eq. (19) is modified to

$$m_a \frac{d\mathbf{v}_a}{dt} = 2 \sum_b V_a V_b \tilde{p}_{ab} \nabla_a^0 W_{ab}^{h^S} + \mathbf{g} + \mathbf{f}_a^{F:p}(h^F) + \mathbf{f}_a^{F:v}(h^F), \quad (29)$$

where h^S denotes the smoothing length used for solid structure. Note that, for the calculation of fluid-structure interaction forces, we use h^F with assumption $h^F \geq h^S$. This will ensure that a fluid particle i can be searched and tagged as a neighboring particle of a solid particle a which is located in the neighborhood of particle i . In detail, the forces $\mathbf{f}_i^{S:p}(h^F)$ and $\mathbf{f}_i^{S:v}(h^F)$ of Eqs. (21) and (25) are modified to

$$\mathbf{f}_i^{S:p}(h^F) = -2 \sum_a V_i V_a \frac{p_i \rho_a^d + p_a^d \rho_i}{\rho_i + \rho_a^d} \nabla_i W(\mathbf{r}_{ia}, h^F), \quad (30)$$

and

$$\mathbf{f}_i^{S:v}(h^F) = 2 \sum_a \eta V_i V_a \frac{\mathbf{v}_i - \mathbf{v}_a^d}{r_{ia}} \frac{\partial W(\mathbf{r}_{ia}, h^F)}{\partial r_{ia}}. \quad (31)$$

Accordingly, the fluid forces exerting on the solid structure $\mathbf{f}_a^{F:p}(h^F)$ and $\mathbf{f}_a^{F:v}(h^F)$ can be obtained straightforwardly.

3.2. Multiple time steps

Here, the dual-criteria time-stepping method [41] is employed for integrating the fluid equations. Two time-step criteria, namely the advection criterion Δt_{ad}^F and the acoustic criterion Δt_{ac}^F , respectively, are

$$\Delta t_{ad}^F = 0.25 \min \left(\frac{h^F}{|\mathbf{v}|_{max}}, \frac{h^F}{\eta} \right), \quad (32)$$

and

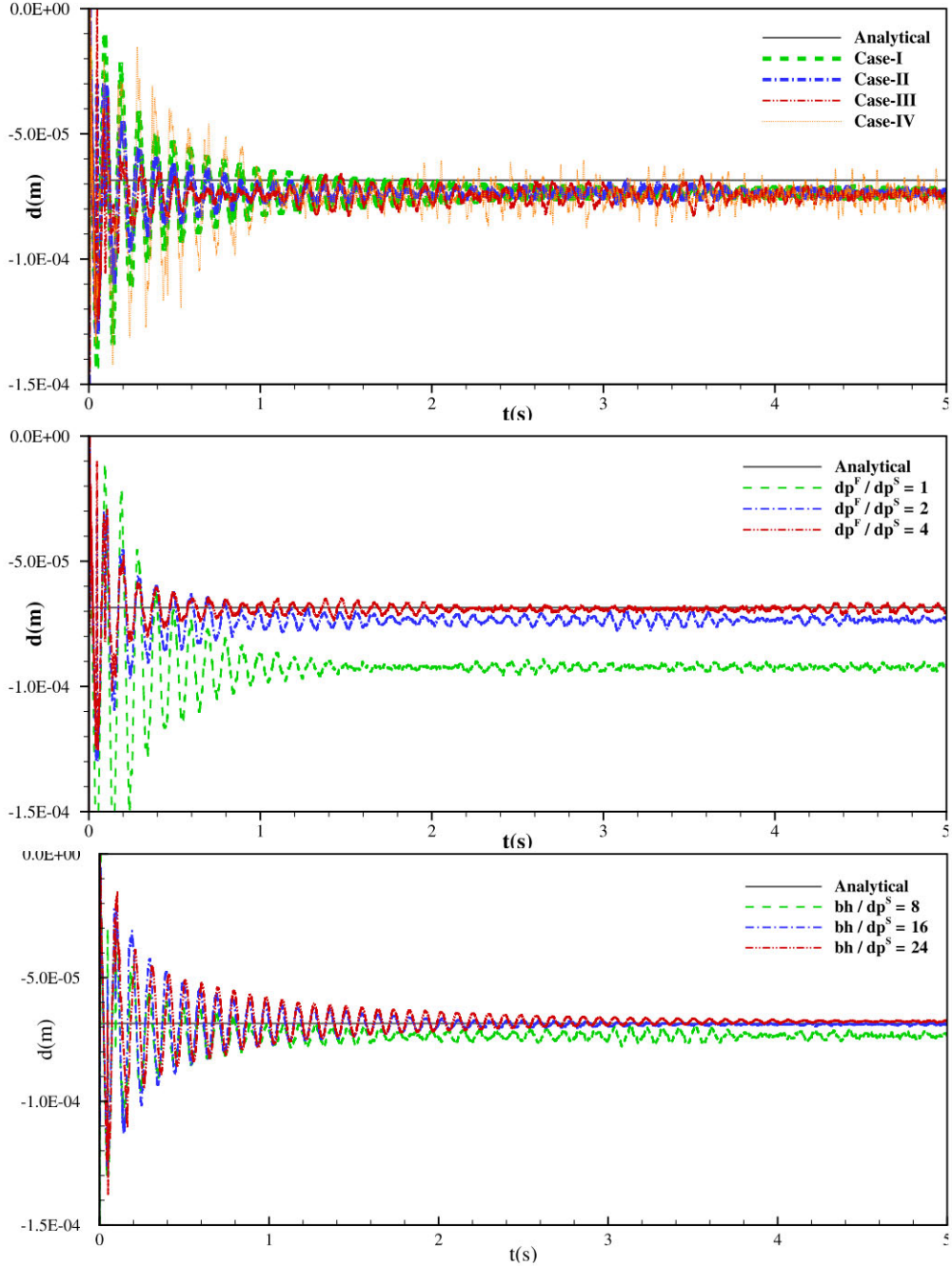


Fig. 3. Results of the mid-span displacement of an elastic plate under a hydrostatic water column for the cases (top panel) given in Table 1, (middle panel) fixed fluid spatial resolution $dp^F = bh/4$ and variable fluid-structure resolution ratios, and (bottom panel) with convergence study at $dp^F/dp^S = 2$.

Table 3

Flow-induced vibration of a flexible beam attached to a rigid cylinder: the setup of different cases.

Cases	dp^F/dp^S	dp^S	Time steps	Number of particles
I	1.0	$dp^S = bh/4.0$	Multiple	21664
II	1.0	$dp^S = bh/8.0$	Multiple	78200
III	2.0	$dp^S = bh/4.0$	Multiple	6880
IV	2.0	$dp^S = bh/4.0$	Single	6880

$$\Delta t_{ac}^F = 0.6 \min \left(\frac{h^F}{c^F + |\mathbf{v}|_{max}} \right). \quad (33)$$

Here, the advection criterion controls the updating of the particle-neighbor list and the corresponding computation of the kernel values and gradients, and the acoustic criterion determines the time integration of the particle motion. The time-step

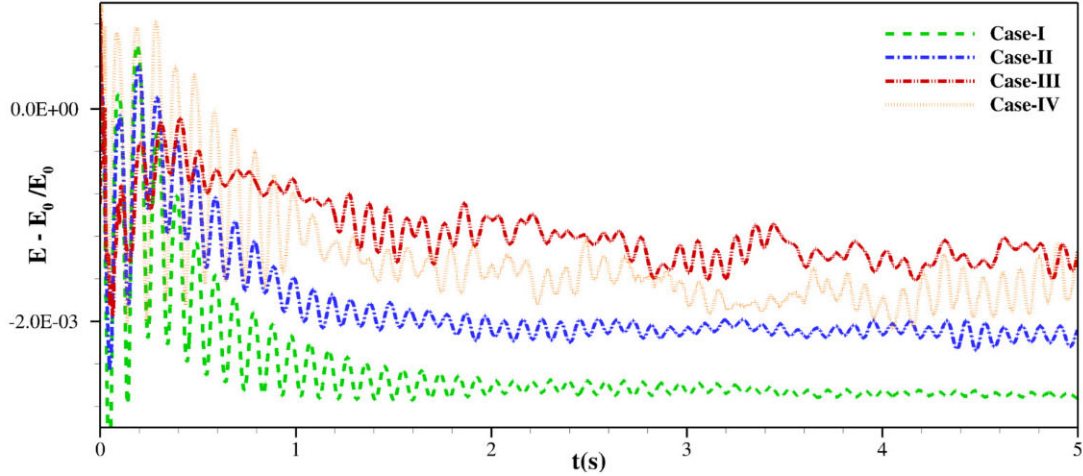


Fig. 4. The time history of the normalized total energy an elastic plate under a hydrostatic water column.

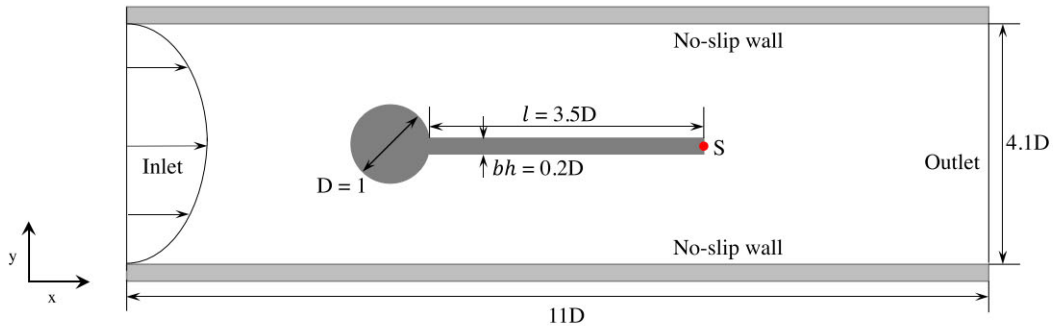


Fig. 5. Sketch of the two dimensional flow-induced vibration of a flexible beam attached to a rigid cylinder with a trajectory sensor S located at the free-end of the beam.

criterion for the solid structure is given as

$$\Delta t^S = 0.6 \min \left(\frac{h^S}{c^S + |\mathbf{v}|_{max}}, \sqrt{\frac{h^S}{|\frac{d\mathbf{v}}{dt}|_{max}}} \right). \quad (34)$$

Generally, $\Delta t^S < \Delta t_{ac}^F$, due to the fact that $c^S > c^F$. Other than choosing Δt^S as the single time step for both fluid and structure, we carry out the structure time integration $\kappa = [\frac{\Delta t_{ac}^F}{\Delta t^S}] + 1$ times, where $[\cdot]$ represents the integer operation, during one acoustic time step of fluid integration. As different time steps are applied in the integration of fluid and solid equations, the issue of force mismatch in the fluid-structure interaction may be encountered. That is, in the imaginary pressure and velocity calculation, the velocity and acceleration of solid particles in Eq. (23) may present several different values updated after each Δt^S . Another issue is that the momentum conservation in the fluid and structure coupling may be violated. To address the force-calculation mismatch, we redefine the imaginary pressure p_a^d and velocity \mathbf{v}_a^d in Eqs. (30) and (31) as

$$\begin{cases} p_a^d = p_i + \rho_i \max(0, (\mathbf{g} - \frac{d\mathbf{v}_a}{dt}) \cdot \mathbf{n}^S) (\mathbf{r}_{ia} \cdot \mathbf{n}^S) \\ \mathbf{v}_a^d = 2\mathbf{v}_i - \tilde{\mathbf{v}}_a \end{cases}, \quad (35)$$

where $\tilde{\mathbf{v}}_a$ and $\frac{d\mathbf{v}_a}{dt}$ represents the single averaged velocity and acceleration of solid particles during a fluid acoustic time step.

3.3. Position-based Verlet scheme

Instead of starting with a half step for velocity followed by a full step for position and another half step for velocity as in the velocity-based Verlet scheme [40], the position-based Verlet does the opposite: a half step for position followed by a full step for velocity and another half step for position. Fig. 1 depicts the velocity- and position-based Verlet schemes assuming that $\kappa = 4$ for the integration of fluid and solid equations. Note that since the position is updated twice and the velocity once with the acceleration at the half step, using the Taylor expansion one can find that the position-based scheme has the same 2nd-order accuracy as the original one.

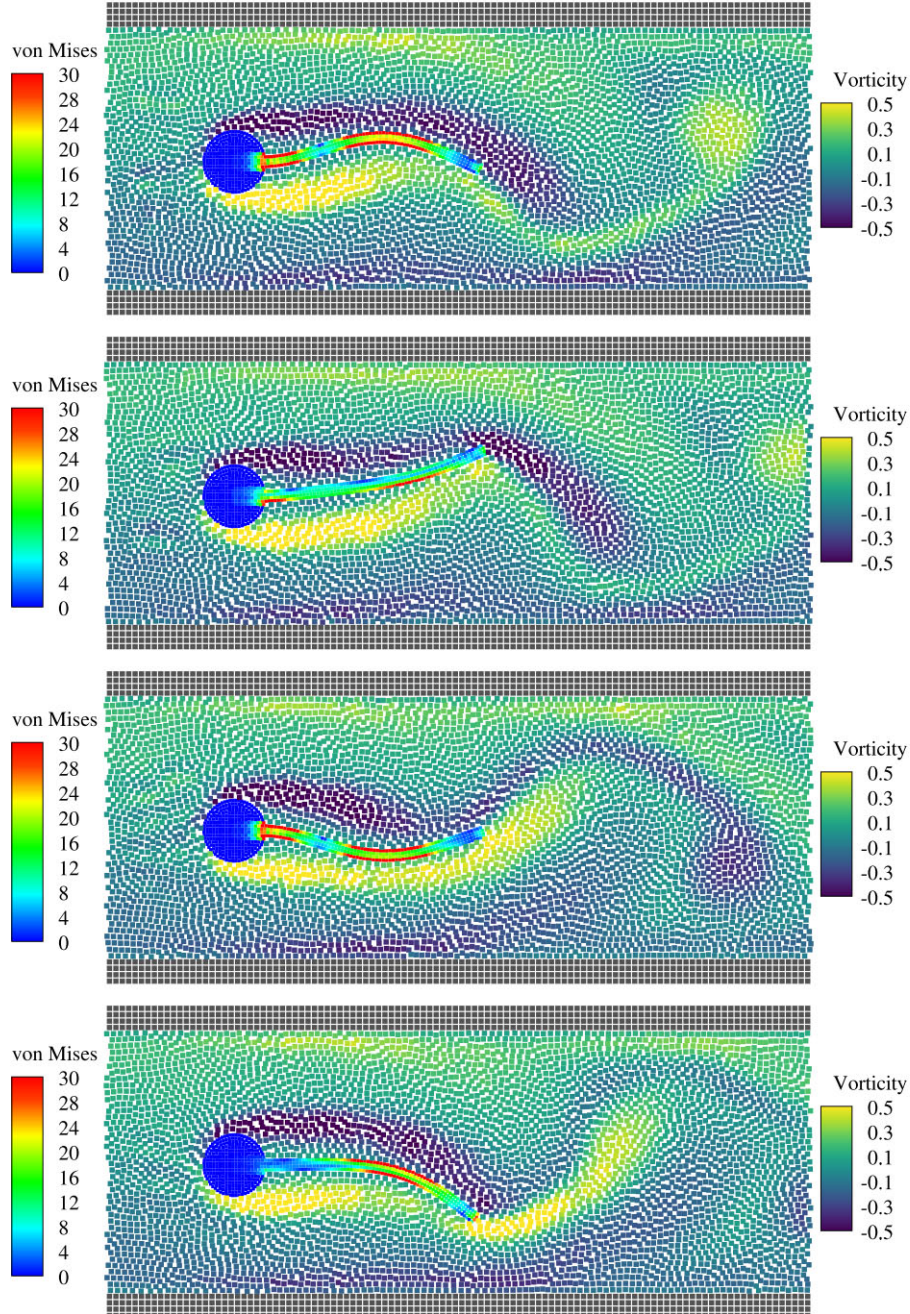


Fig. 6. Flow-induced vibration of a beam attached to a cylinder with $d^F/d^S = 2.0$ (Case-III): the flow vorticity field and beam deformation at four time instants labeled by red dots in Fig. 7. (For interpretation of the colors in the figure(s), the reader is referred to the web version of this article.)

Table 4

Flow-induced vibration of a beam attached to a cylinder: computational efficiency and predicted amplitude and frequency. The computer information is similar with that given in Table 2. To analyze the computational performance, we evaluate the CPU wall-clock time until the dimensionless time of 200.

Cases	Amplitude in y-axis	Frequency	CPU time (s)
I	0.89	0.180	1297.7
II	0.86	0.184	10926.7
III	0.86	0.188	249.5
IV	0.86	0.188	451.4

Here, we denote the values at the beginning of a fluid acoustic time step by superscript n , at the mid-point by $n + \frac{1}{2}$ and eventually at the end of the time-step by $n + 1$. At first, the integration of the fluid is conducted as

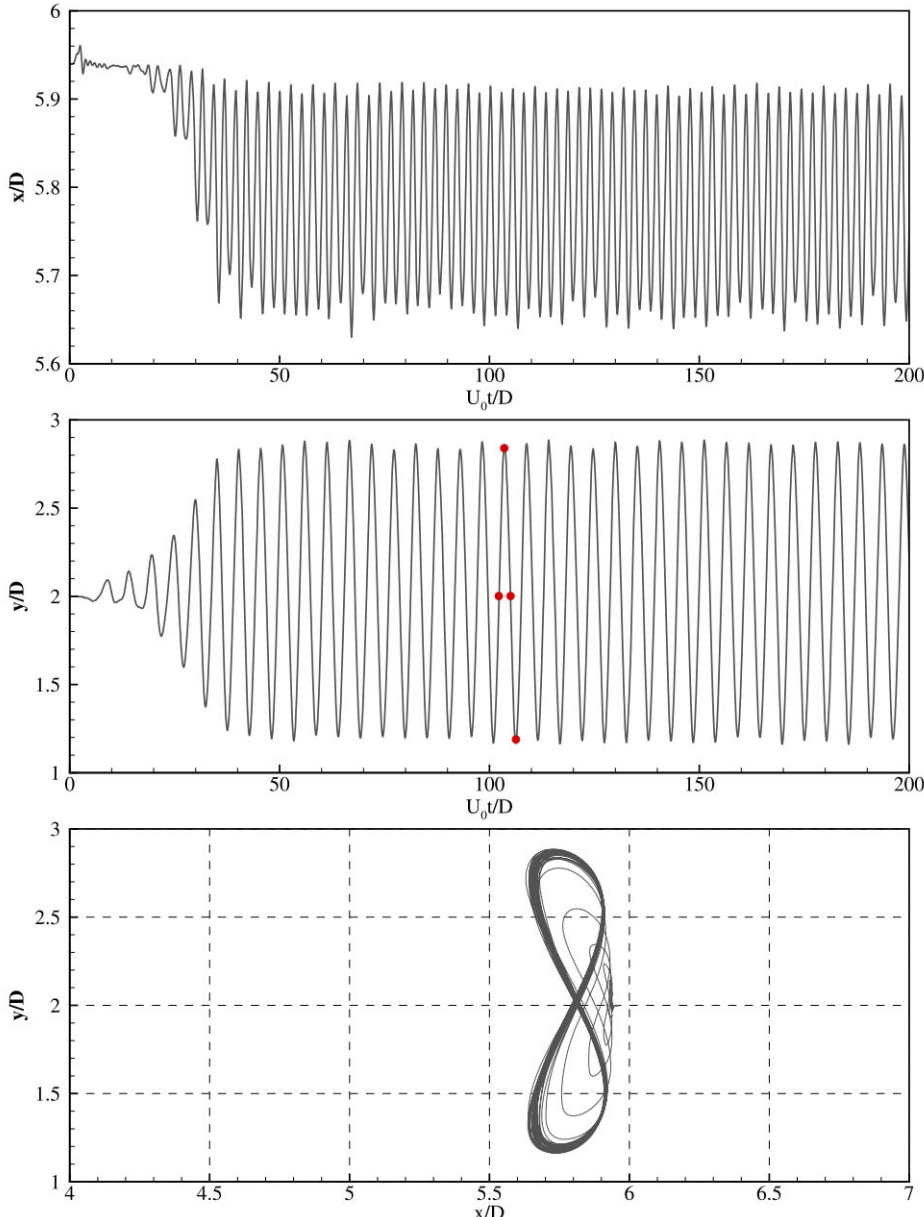


Fig. 7. Flow-induced vibration of a beam attached to a cylinder (Case-III): amplitude of the displacement in x -direction (top panel), amplitude of the displacement in y -direction (middle panel) and the trajectory (bottom panel) of point S .

Table 5

Flow-induced vibration of a beam attached to a cylinder: convergence study of Case-III.

Spatial resolution	Amplitude in y -axis	Frequency
$bh/dp^S = 4$	0.860	0.188
$bh/dp^S = 8$	0.856	0.189
$bh/dp^S = 16$	0.855	0.189

Table 6

Dam-break flow through an elastic gate: basic setup of different cases.

Cases	dp^F/dp^S	dp^S	Time steps	Number of particles
I	1.0	$dp^S = b/4.0$	Multiple	14144
II	1.0	$dp^S = b/8.0$	Multiple	47394
III	2.0	$dp^S = b/4.0$	Multiple	5220
IV	2.0	$dp^S = b/4.0$	Single	5220

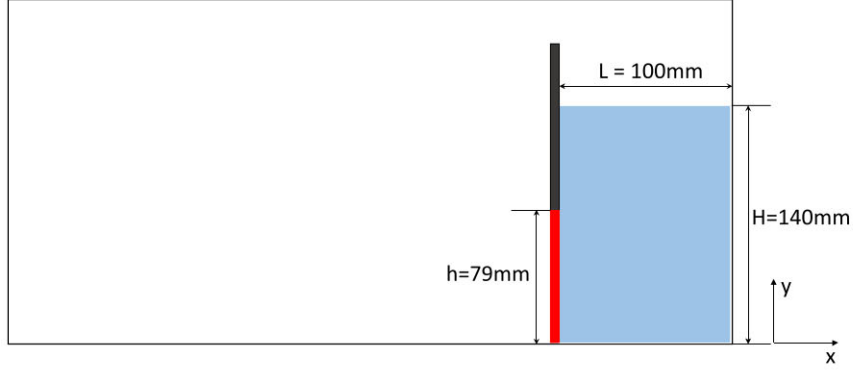


Fig. 8. Sketch of the dam-break flow through an elastic gate which has a width of $b = 5\text{ mm}$.

Table 7

Dam-break flow through an elastic gate: computational efficiency. The computer information is similar with that given in Table 2 and we evaluate the CPU wall-clock time for computation until the time of 0.4.

Cases	I	II	III	IV
CPU time (s)	80.15	523.17	27.17	130.77

$$\begin{cases} \rho_i^{n+\frac{1}{2}} = \rho_i^n + \frac{1}{2} \Delta t_{ac}^F \frac{d\rho_i}{dt} \\ \mathbf{r}_i^{n+\frac{1}{2}} = \mathbf{r}_i^n + \frac{1}{2} \Delta t_{ac}^F \mathbf{v}_i^n \end{cases}, \quad (36)$$

by updating the density and position fields into the mid-point. Then particle velocity is updated to the new time step in the following form

$$\mathbf{v}_i^{n+1} = \mathbf{v}_i^n + \Delta t_{ac}^F \frac{d\mathbf{v}_i}{dt}. \quad (37)$$

Finally, the position and density of fluid particles are updated to the new time step by

$$\begin{cases} \mathbf{r}_i^{n+1} = \mathbf{r}_i^{n+\frac{1}{2}} + \frac{1}{2} \Delta t_{ac}^F \mathbf{v}_i \\ \rho_i^{n+1} = \rho_i^{n+\frac{1}{2}} + \frac{1}{2} \Delta t_{ac}^F \frac{d\rho_i}{dt} \end{cases}. \quad (38)$$

At this point, the pressure and viscous forces induced acceleration of solid particles are considered as constant during the integration for solid particles. For convenience of explanation, index $\kappa = 0, 1, \dots, \kappa - 1$ is used to denote a integration step for solid particles. With the position-based Verlet scheme, the deformation tensor, density and particle position are updated to the midpoint as

$$\begin{cases} \mathbb{F}_a^{\kappa+\frac{1}{2}} = \mathbb{F}_a^\kappa + \frac{1}{2} \Delta t^S \frac{d\mathbb{F}_a}{dt} \\ \rho_a^{\kappa+\frac{1}{2}} = \rho_a^0 \frac{1}{J} \\ \mathbf{r}_a^{\kappa+\frac{1}{2}} = \mathbf{r}_a^\kappa + \frac{1}{2} \Delta t^S \mathbf{v}_a \end{cases}. \quad (39)$$

Then the velocity is updated by

$$\mathbf{v}_a^{\kappa+1} = \mathbf{v}_a^\kappa + \Delta t^S \frac{d\mathbf{v}_a}{dt}. \quad (40)$$

At final stage, the deformation tensor and position of solid particles are updated to the new time step of solid structure with

$$\begin{cases} \mathbb{F}_a^{\kappa+1} = \mathbb{F}_a^{\kappa+\frac{1}{2}} + \frac{1}{2} \Delta t^S \frac{d\mathbb{F}_a}{dt} \\ \rho_a^{\kappa+1} = \rho_a^0 \frac{1}{J} \\ \mathbf{r}_a^{\kappa+1} = \mathbf{r}_a^{\kappa+\frac{1}{2}} + \frac{1}{2} \Delta t^S \mathbf{v}_a^{\kappa+1} \end{cases}. \quad (41)$$

Before starting the next fluid step, the time integration of solid particles, which is depicted by Eqs. (39) to (41), is iterated κ times. The detailed algorithms of the present multi-resolution SPH method are given in Algorithm 1. The fluid density reinitialization for free-surface flows, when there exist solid particles within the particle support domain, is given as

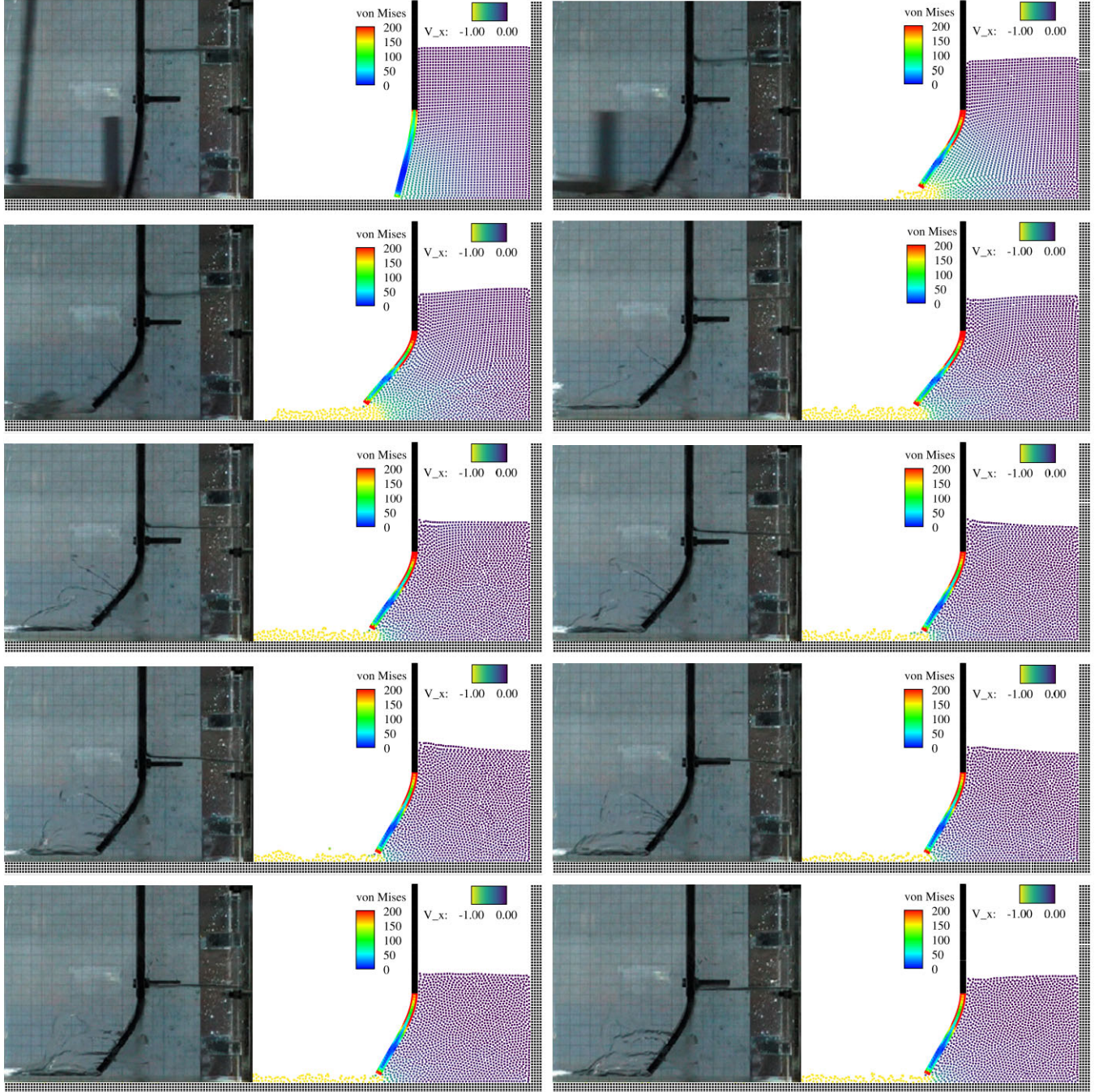


Fig. 9. Dam-break flow through an elastic gate: snapshots from Case-III are compared against experimental frames presented by Antoci et al. [12] at every 0.04s starting from $t = 0.04s$.

$$\rho_i = \max \left(\rho_i^*, \rho_i^0 \frac{\sum_j W(\mathbf{r}_{ij}, h^F) + \sum_a W(\mathbf{r}_{ia}, h^F) \frac{V_j^0}{V_i^0}}{\sigma^0} \right), \quad (42)$$

where ρ^* denotes the density before re-initialization, ρ^0 and $\sigma^0 = \sum_j W^0(\mathbf{r}_{ij}, h^F)$ are the initial density and the reference particle number density, respectively. For flows without free surface, Eq. (42) is simplified to

$$\rho_i = \rho_i^0 \frac{\sum_j W(\mathbf{r}_{ij}, h^F) + \sum_a W(\mathbf{r}_{ia}, h^F) \frac{V_j^0}{V_i^0}}{\sigma^0} \quad (43)$$

Note that in Eqs (42) and (43) V_j^0/V_i^0 is the initial volume ratio between fluid and solid particle.

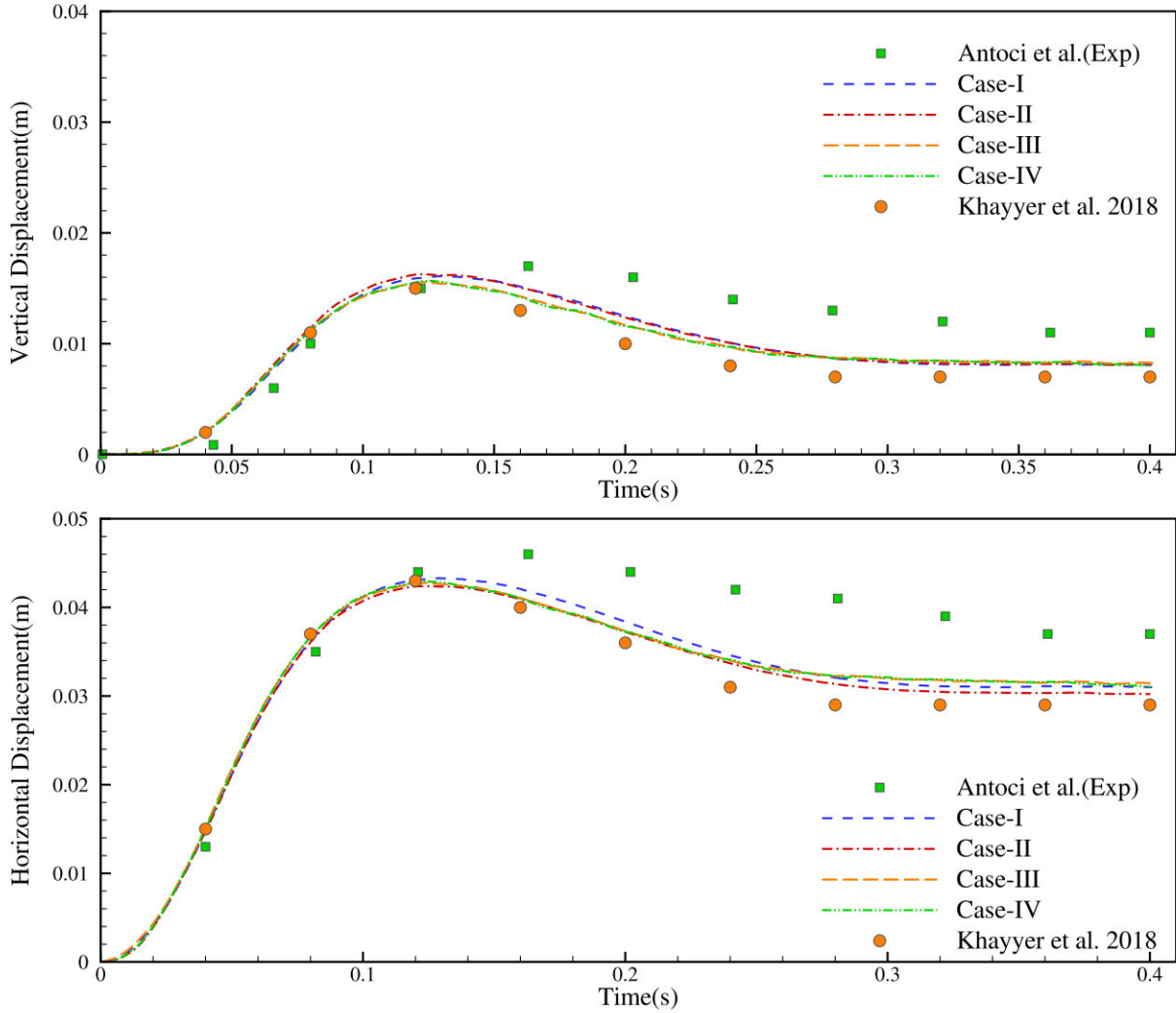


Fig. 10. Dam-break flow through an elastic gate: horizontal (top panel) and vertical (bottom panel) displacement of the free end of the plate. Computational results are compared with experimental data provided by Antoci et al. [12] and previous numerical results of Ref. [21] (with $\nu = 0.4$). Similar to previous simulations [21,19,25], small differences are observed between the present numerical results and the experiment data during the closing period, and these discrepancies maybe associated to the different material models [25].

In the position-based Verlet scheme, as the velocity field is updated only once in the current fluid acoustic time step criterion, time marching of the momentum equations for fluid and solid are exactly consistent as the velocity marching interval $(\Delta t_{ac}^F)_n = \sum_{\kappa=0}^{\kappa-1} (\Delta t^S)_\kappa$, as shown Fig. 1. Therefore, the position-based Verlet algorithm achieves strict momentum conservation in fluid-structure coupling, when multiple time steps are employed. In contrast, the velocity-based Verlet scheme does not guarantee momentum conservation as $0.5 [(\Delta t_{ac}^F)_{n-1} + (\Delta t_{ac}^F)_n] \neq 0.5 [\sum_{\kappa=0}^{\kappa-1} ((\Delta t^S)_{\kappa-1} + (\Delta t^S)_\kappa)]$, as also shown in Fig. 1.

4. Numerical examples

In this section, we first study three benchmarks, where the structures may experience large deformation due to either flow-induced vibration or time-dependent water pressure, to validate the accuracy and computational efficiency of the present method. Having the validation studies presented, we then demonstrate the versatility of the method for applications in bio-mechanical system, i.e. venous valve and passive flapping of fish-like body. In all the following examples, the 5th-order Wendland smoothing kernel function with the smoothing lengths $h^F = 1.3dp^F$ and $h^S = 1.3dp^S$, where dp^F and dp^S represent the initial particle spacing for fluid and solid structure, are employed.

4.1. Hydrostatic water column on an elastic plate

The first benchmark test we consider herein is the deformation of an elastic plate under hydrostatic pressure of a water column. Following Fourey et al. [42] and Khayyer et al. [21], an aluminum plate with the thickness $bh = 0.05$ m, density $\rho_S = 2700$ kg/m³, Young's modulus $E = 67.5$ GPa and Possion ratio $\nu = 0.34$, is suddenly exposed to a 2m height water

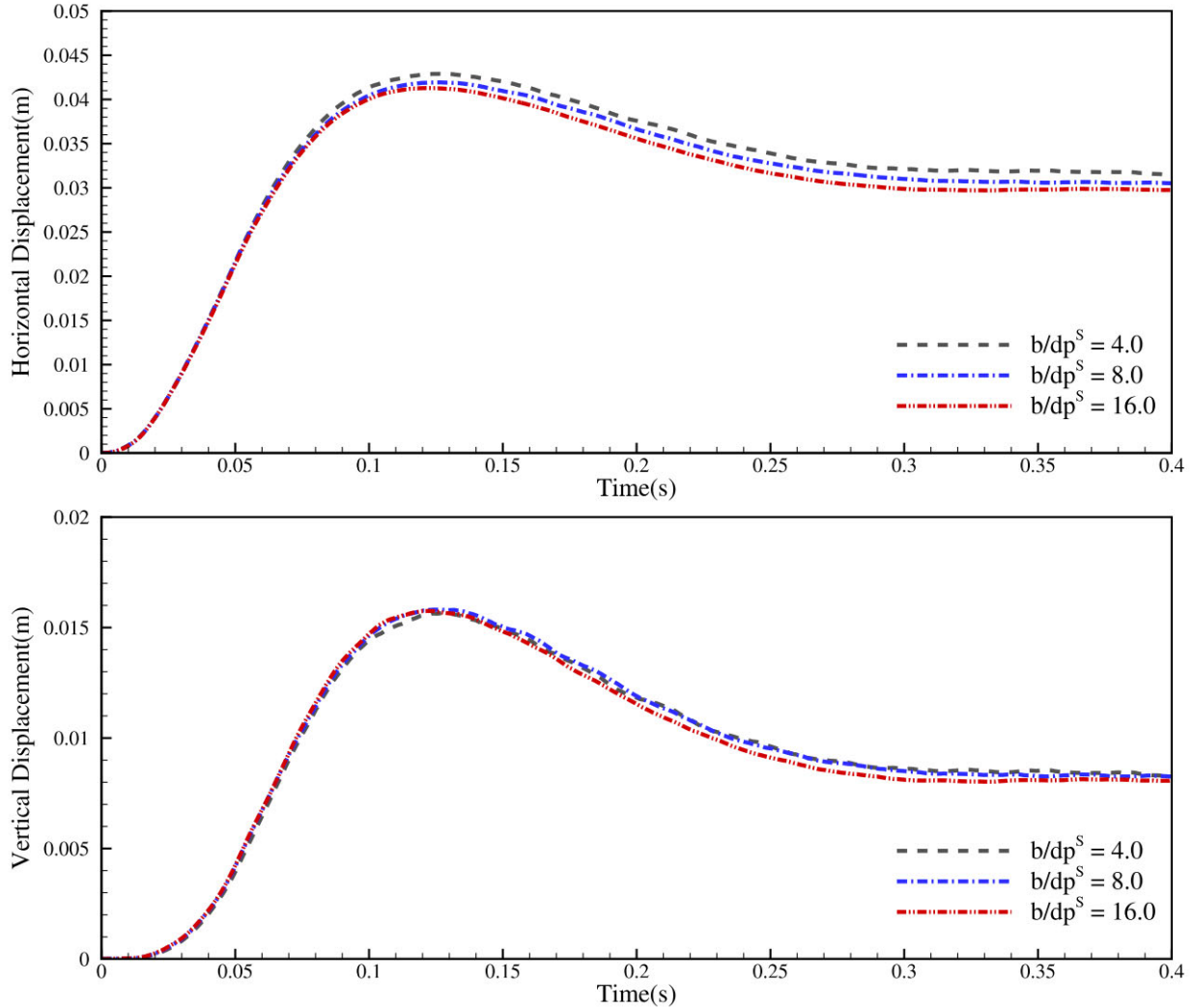


Fig. 11. Convergence study for Case-III: horizontal displacement of the free end of the plate (top panel) and vertical displacement of the free end of the plate (bottom panel).

Algorithm 1: The multi-resolution SPH method for FSI problems.

```

1 Setup parameters and initialize the simulation;
2 Compute the initial number density of fluid particles;
3 Compute the normal direction of structure surface;
4 Obtain the corrected configuration for the solid particles;
5 while simulation termination condition is not satisfied do
6   Get the fluid advection time step  $\Delta t_{ad}^F$ ;
7   Reinitialize the fluid density;
8   Update the normal direction of the solid structure;
9   while  $\sum \Delta t_{ac}^F \leq \Delta t_{ad}^F$  do
10    Get the fluid acoustic time step  $\Delta t_{ac}^F$ ;
11    Integrate the fluid equations with the position-based Verlet scheme;
12    Compute the pressure and viscous forces exerting on structure due to fluid;
13    while  $\sum \Delta t_{ac}^S \leq \Delta t_{ad}^F$  do
14     Get the time step  $\Delta t_{ac}^S$  of solid structure;
15     Integrate the solid equations with the position-based Verlet scheme;
16    end
17    Compute the time-averaged velocity and acceleration of solid structure;
18  end
19  Update the particle-neighbor list and kernel values and gradient for fluid particles ;
20  Update the particle configuration between the fluid and solid particles ;
21 end
22 Terminate the simulation.

```

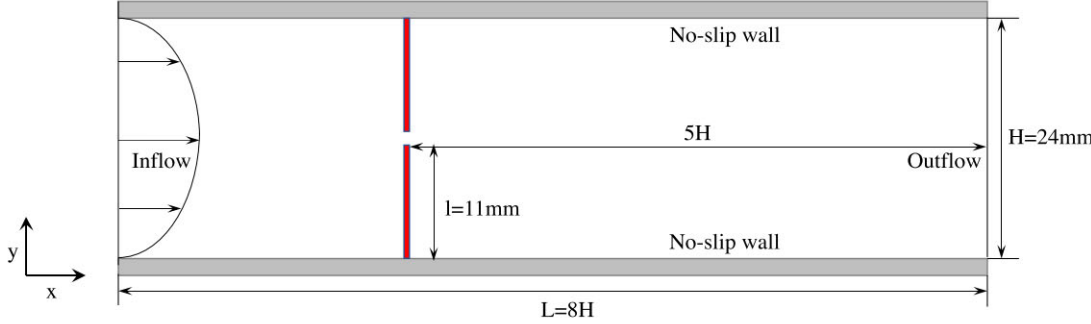


Fig. 12. Sketch of the computational setup for the two dimensional idealized vein with flexible valve leaflets.

column as shown in Fig. 2. According to Refs. [42,21], an equilibrium state reaches after initial oscillations and the predicted equilibrium displacement at the plate mid-span from an analytical model is $d = -6.85 \times 10^{-5}$ m. Following Khayyer et al. [21], a constant fluid time-step size $\Delta t^F = 2.0 \times 10^{-5}$ s is used here, and we compute the problem until time $t = 5$ s.

As shown in Table 1, four cases with **fixed structure resolution, different fluid-structure resolution ratios** and single or multiple time steps are considered to study the computational accuracy and efficiency. It is observed in Fig. 3 that all computations are numerically stable and the final displacements predicted with multiple time steps are in quite good agreement with the results in Ref. [21] obtained at the same structure resolution (see their Fig. 8), but show more sustained initial oscillations and a slightly more accurate displacement. Note that the more sustained initial oscillations indicate that the present method preserves more energy and has less numerical dissipation.

Table 2 summarizes the computation time for the four cases. **Note that, since the structure resolution is constant, the computation time cost associated with the structure is also constant.** Therefore, the improved computational efficiency is obtained from the reduction in the computations associated to fluid. Again, since a constant time step size is used for the computation of fluid equations, this is evidently found in Table 2 that, for this benchmark problem, the speedup is about 60 (Case-III to Case-IV) if only multiple time steps are used. Furthermore, the overall speedup of fluid computation, compared to the single time steps computation corresponding to Case-I, is about 240 when $dp^F/dp^S = 2$, and about 960 when $dp^F/dp^S = 4$. We did not carry out such computations due to the tremendous computational costs.

Another interesting observation is that, while the single time step computation obtains stable solution, the residual oscillation (similar to the results in Ref. [42] but with smaller magnitude) is much larger than that obtained with multiple time steps. Our numerical tests show that such discrepancy only happens for this benchmark problem. The reasons probably include the extreme impedance mismatch due to the extreme ratio between solid and fluid sound speeds, and the lack of physical viscosity or damping for the liquid and structure, respectively. This observation also suggests that multiple time steps are able to regularize the solution and are hence more desirable, even when the computation efficiency is not an issue.

One can also observe that the increasing resolution ratio does not change the final mid-span displacement but leads to less regular oscillations. **This behavior indicates that the accuracy of the mid-span displacement is determined by the structure resolution, which is fixed here,** and the regularity or accuracy of oscillation by the fluid resolution. To further study the influence of the resolution ratio, we consider several cases with fixed fluid resolution. As shown in Fig. 3, while the accuracy of the predicted displacement increases with the resolution ratio, the oscillation regularity stays almost the same because of the fixed fluid resolution. **These two observations are in agreement with each other and suggest that the resolutions of fluid and structure determines different aspects of accuracy.** Note that, it is not desirable to use too extreme resolution ratios, as this may lead to very low fluid resolutions and makes it difficult to maintain its corresponding accuracy. Therefore, **for the rest of this paper only the resolution ratio of $dp^F/dp^S = 2$ is used.**

Another notable observation from the results with increased structure resolutions is that an approximately 2nd-order convergence is achieved for the middle-span displacement. To clarify this observation, a convergence study is carried out with increasing both structure and fluid spatial resolution at $dp^F/dp^S = 2$. The obtained results shown in Fig. 3 confirm such high-order convergence of the middle-span displacement.

To validate the energy conservation property of the proposed method, the time history, as shown in Fig. 4, of the normalized total energy of the system has been recorded for all the cases given in Table 1. Similar to Ref. [21], the normalized total energy shows a small drop due to numerical viscosity, and gives a value varying from -1.0×10^{-3} to -2.5×10^{-3} for different cases after a regular oscillation process. These values are in good agreement with that of Ref. [21] which reported a value about -2.0×10^{-3} . Note that, more energy is conserved in the multi-resolution scenario as the fluid spatial resolution decrease, which may be due to the fact that less numerical viscosity is presented at coarse spatial resolution.

4.2. Flow-induced vibration of an elastic beam behind a cylinder

In this section, we consider a two dimensional flow-induced vibration of a flexible beam attached to a rigid cylinder. Following Turek and Hron [43] and Han and Hu [17], the geometric parameters and basic setup of the problem are depicted in Fig. 5. The rigid cylinder is centered at $(2D, 2D)$ with $D = 1$ measured from the left bottom corner of the computational

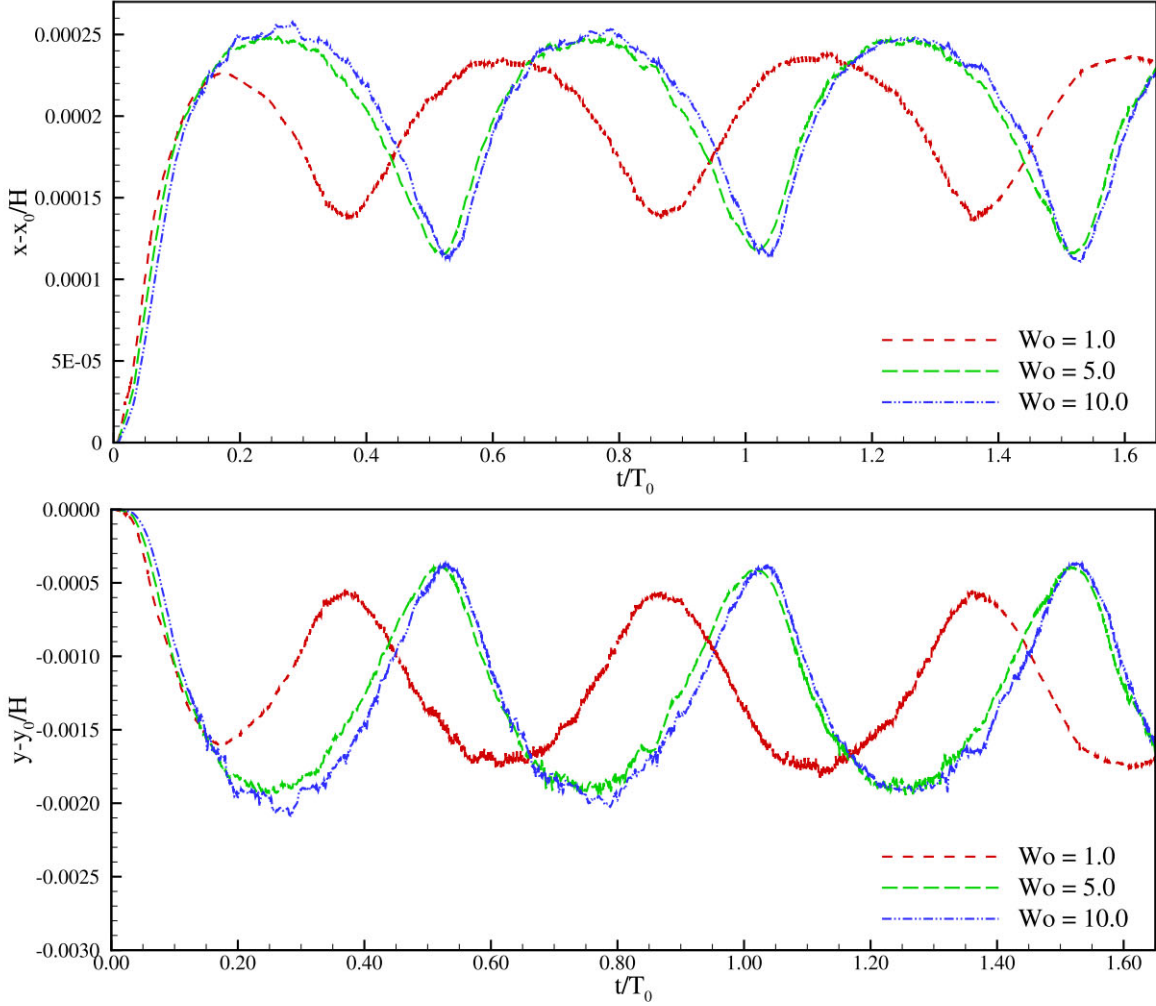


Fig. 13. Pulsatile flow through venous valve leaflets: horizontal displacement (top panel) and vertical displacement (bottom panel) of the free-end of the top leaflet. Computational results for three Womersley numbers are presented.

domain. No-slip boundary condition is imposed on the top and bottom walls, while inflow and outflow boundary conditions are employed at the left and right sides of the domain, respectively. The inflow condition is realized by imposing a velocity profile [43,17] of $U(y) = 1.5\bar{U}(t, y)(H - y)y/H^2$, where $\bar{U}(t, y) = 0.5U_0(1.0 - \cos(0.5\pi t))$ if $t \leq t_s$ otherwise $\bar{U}(t, y) = U_0$, with $U_0 = 1.0$ and $t_s = 2.0$. Similar to Refs. [43,17], the physical parameters are chosen to setup a challenging test, which consists of a quite flexible beam. The density ratio of the structure to the fluid is $\rho^S/\rho^F = 10$ and the Reynolds number $Re = \rho^F U_0 D / \eta = 100$. The isotropic linear elastic model is employed with the dimensionless Young's modulus $E^* = E/\rho^F U_0^2 = 1.4 \times 10^3$, and the Poisson ratio $\nu = 0.4$. We consider four cases with different fluid-structure resolution ratios and single or multiple time steps as shown in Table 3 to study the computational efficiency and accuracy.

Fig. 6 shows the flow vorticity field and beam deformation for Case-III at different time instants in a typical periodic movement when self-sustained oscillation is reached. Good agreements with previous computational results [43,17,44] are noted. Fig. 7 gives the time dependent position of the trajectory sensor S . It is observed that the beam reaches a periodic self-sustained oscillation as time goes beyond a dimensionless time of 50. The trajectory of point S shows a typical Lissajous curve with a frequency ratio of 2 : 1 between horizontal and vertical motions [44], implying a good agreement with the computational results of both Refs. [44] and [45]. Table 4 gives the dimensionless amplitude of the oscillation in y direction, and the frequency obtained from the cases given in Table 3. Compared with the previous results in the literature [43–45,41], where the frequency is predicted as 0.19 and the amplitude is varied from 0.78 to 0.92, good agreement is noted. It can also be observed that with the resolution ratio of $dp^F/dp^S = 2.0$, one is able to obtain a speedup of 5.2 (Case-III to Case-I) without notable compensation on numerical accuracy. Note that, an extra speedup of 1.8 (Case-III to Case-IV) can be further achieved compared with single time step computation. Also note that, since the structure computation time is about the same for Case-I and Case-III, one can easily find the overall speedup of fluid computation of Case-III is about 20, compared to the single time steps computation corresponding to Case-I.

To further evaluate the convergence of the present method, we performed simulations with increasing the spatial resolution. It is found that the amplitude and the frequency converge to 0.855 and 0.189, respectively, as noted in Table 5.

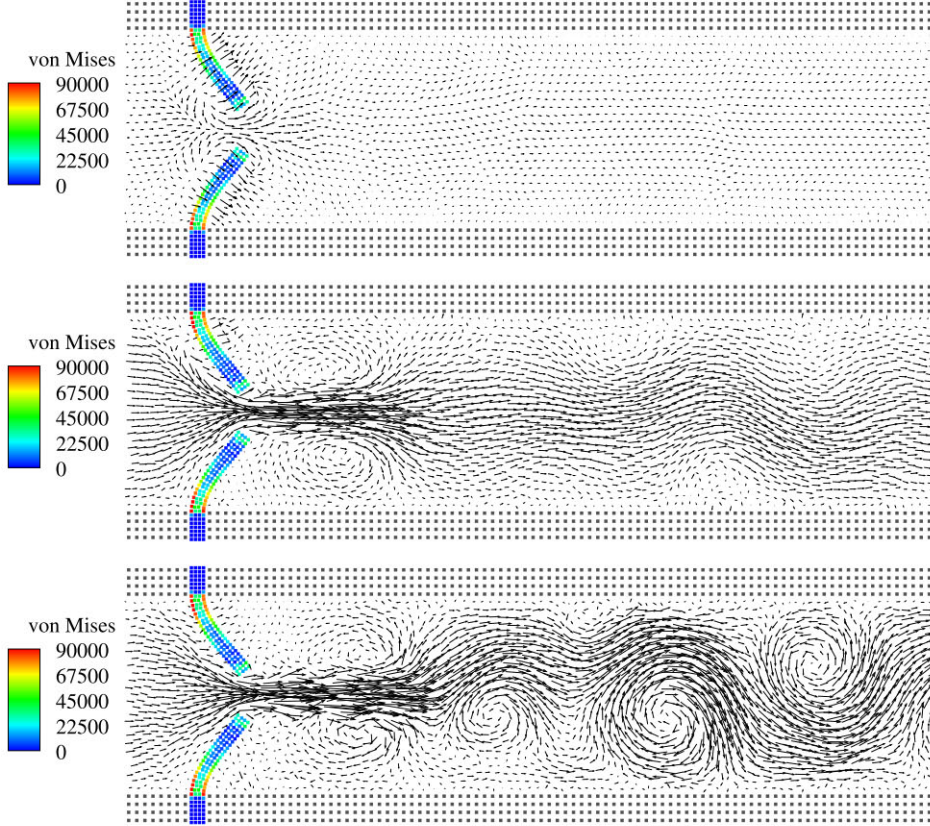


Fig. 14. Pulsatile flow through venous valve leaflets: deformation of leaflets colored by von Mises stress and velocity vectors of the flow. Computational results for three Womersley numbers are presented, viz. $W_0 = 1.0$ (top panel), $W_0 = 5.0$ (middle panel) and $W_0 = 10.0$ (bottom panel).

Compared with the converged results, the present method demonstrates good accuracy except with the slightly overestimated amplitude in y -direction.

4.3. Dam-break flow through an elastic gate

In this section, we consider the deformation of an elastic plate subjected to time-dependent water pressure, where free-surface flow is involved. Following the experiment study conducted by Antoci et al. [12], the configuration is shown in Fig. 8 where an elastic plate is clamped at its upper end and is free at the lower one, interacting with a bulk of water initially confined in an open-air tank behind it. Following Ref. [12], the fluid flow is considered to be inviscid with the density $\rho^F = 1000 \text{ kg/m}^3$. The elastic plate corresponds to rubber and the linear isotropic model is employed with the properties of density $\rho^S = 1100 \text{ kg/m}^3$, Young's modulus $E = 7.8 \text{ MPa}$ and Possion ratio $\nu = 0.47$. Note that a more realistic Possion ratio ν is chosen herein compared with the numerical setup in Ref. [12] (therein $\nu = 0.4$). The clamp condition is imposed to the upper end of the plate through constraints of the rigid base. Here, similar to the previous problem, four cases as shown in Table 6 are computed to investigate the accuracy and computational efficiency.

The comparison between the snapshots obtained from Case-III and the experiment presented by Antoci et al. [12] is illustrated in Fig. 9. These snapshots correspond to every 0.04s, starting at time $t = 0.04\text{s}$. It can be observed that the simulation shows a free-surface motion quite close to that of the experiment. Note that, the experimental result shown in Fig. 9 present side-wall splashes after $t = 0.08\text{s}$. This is due to a considerable side leakage between the tank wall and the flexible plate [12,20]. Since the present simulation is two dimensional, such splashes are not presented.

The horizontal and vertical displacements of the free end of the plate obtained here are compared against the experiment [12] and previous numerical results in Khayyer et al. [21] in Fig. 10. For all the four cases, good agreements with experimental data and previous results are noted. In the early stages of the dambreak, the horizontal displacement increases quickly due to the initial high water level and static pressure. At time $t = 0.15\text{s}$, the plate reaches its maximum deformation with a horizontal displacement of approximately 0.43. As the water level and static pressure decreases, the plate gradually returns to its equilibrium state which is characterized by the balance between the elastic force and the force introduced by the dynamic water pressure. It also worth noting that similar to previous simulations [21,19,25], small differences are observed between the present results and the experiment data during the closing period. These discrepancies can be associated to the material model employed in the simulations [25].

Compared to the results with single resolution, the multi-resolution computation demonstrates similar fidelity, while showing optimized computational efficiency (speedup of 2.9 for Case III to Case-I) as reported in Table 7. Using multiple

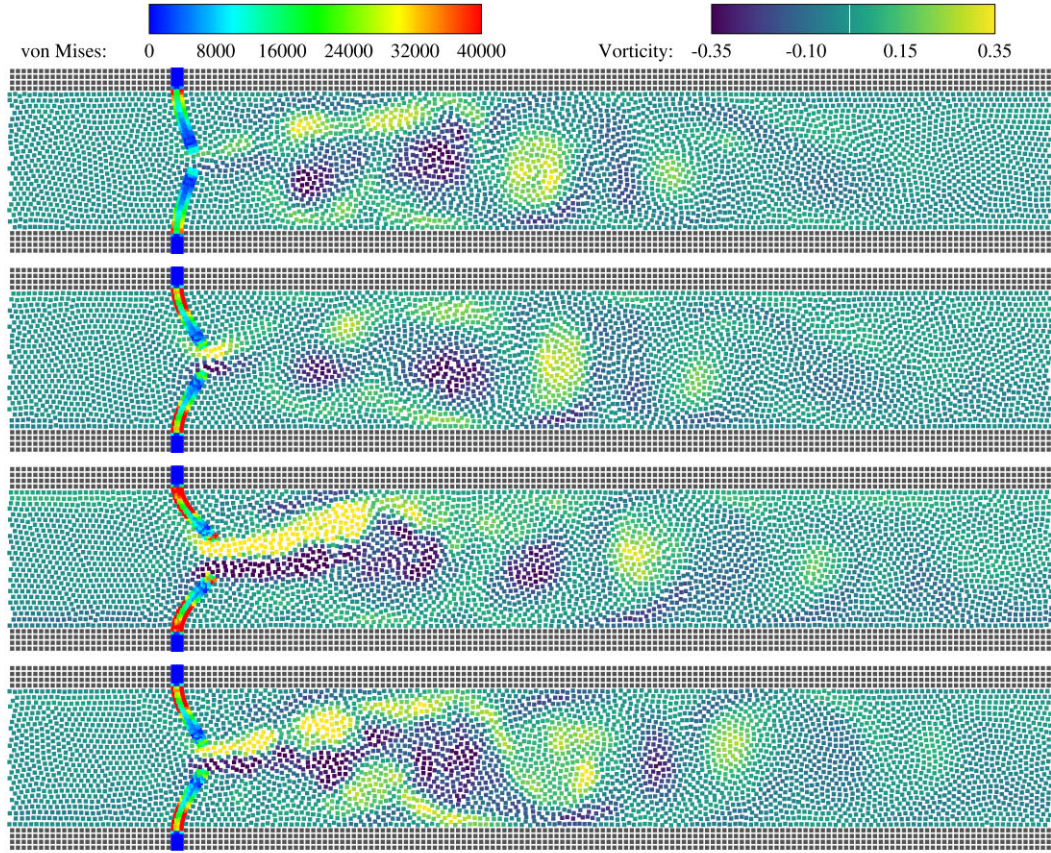


Fig. 15. Pulsatile flow through venous valve leaflets: deformation of leaflets and the corresponding vorticity field at different time instants, viz. $t = 0.62$ s (first panel), $t = 0.65$ s (second panel), $t = 0.75$ s (third panel) and $t = 0.86$ s (last panel). The Womersley number is $W_o = 10.0$.

time steps gives high extra computational performance (speedup of 4.8 for Case-III to Case IV) compared to the single time step cases. Again, the overall speedup of fluid computation of Case-III is about 70 compared to the single time steps computation corresponding to Case-I.

The results from a convergence study are plotted in Fig. 11. Before reaching its maximum deformation, very close behaviors are noted for the three different spatial resolutions. For the horizontal displacement, the maximum deformation decreases slightly as spatial resolution increase, which is consistent with the results obtained with single resolution as shown in Fig. 10.

4.4. Pulsatile flow through venous valve leaflets

Here, we consider a pulsatile flow through a flexible venous valve using a two dimensional idealized geometry to demonstrate the versatility of the present method for practical applications in bio-mechanical system. As depicted in Fig. 12, straight valve leaflets attached to the walls are taken into account and the leaflet thickness is chosen to be $b = 0.2$ mm falling in the range measured by van Langevelde et al. [46] for healthy venous valves. Although the present geometric shape is highly simplified, the investigation reported herein gives the essential flapping behavior of valve leaflets interacting with pulsatile blood flow. The channel walls are assumed to be rigid, and no-slip boundary condition is imposed. Inflow and outflow conditions are applied at the left and right sides of the domain, respectively. The imposed pulsative inflow is characterized by the dimensionless Womersley number, $W_o = \frac{H}{2} \sqrt{\frac{\omega}{\eta}}$, which represents the ratio of the oscillatory inertial effects to the viscous effects, where ω denotes the angular frequency. The velocity profile of the pulsatile blood-like flow is given in Appendix B. The fluid density $\rho^F = 1000$ kg/m³ and the dynamic viscosity varies according to the Womersley number. The Neo-Hookean material model is used for the leaflets with Young's modulus $E = 1.5$ MPa, Poisson's ratio $\nu = 0.49$ and density $\rho^S = 1060$ kg/m³. The initial particle spacing of valve leaflet is set as $dp^S = b/4.0$ and the resolution ratio is $dp^F/dp^S = 2.0$.

We consider three cases with different Womersley numbers, namely, $W_o = 1.0$, 5.0 and 10.0, corresponding to the velocity profiles shown in Fig. 20. Fig. 14 gives the deformation of leaflets colored by the von Mises stress and the corresponding velocity vectors at $t = 2.0$ s. A series of vortices in the downstream of the leaflets can be observed. They are particularly prevalent when the Womersley number is large. Fig. 15 depicts several frames of the flow field colored by vorticity and the deformation of the valve leaflets with $W_o = 10.0$. Four snapshots approximately span a flapping period. Large velocity gradients develop at the tip of the leaflet and a shear layer originates from the tip and separates the re-

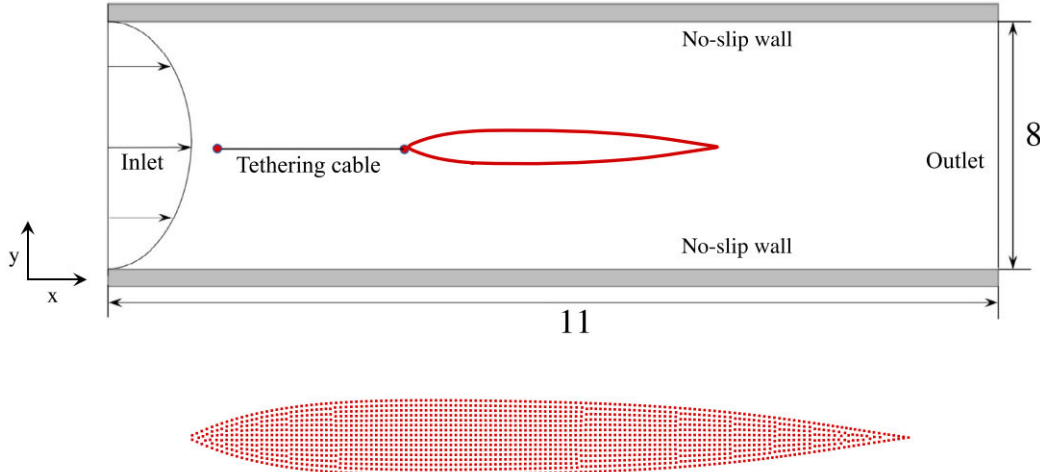


Fig. 16. Schematic diagram of the two dimensional flow induced passive flapping of the **flexible fish-like body**, and the corresponding initial particle distribution of the body.

circulating flow region behind the leaflet from the main flow. The predicted horizontal and vertical displacements of the top leaflet are given in Fig. 13. It is observed that the interactions between the pulsatile flow and the leaflets give rise to self-sustained large-amplitude oscillations with the similar time period of the pulsatile inflow. With increasing Womersley number, large-amplitude oscillations are observed while the period remains unaltered from that of the pulsatile inflow

4.5. Passive flapping of flexible fish-like body

Here, different from previous simulations involving passive flapping of flexible filaments (see e.g. Ref. [47]), the present fish-like body has a foil-like shape and is free except that the head is tethered to a fix point, located at (2.0, 4.0), through a 3.0 long cable. The schematics of the computational setup and the initial particle distribution of the body are shown in Fig. 16. The outline of the body is given by a mirrored 5th order polynomial function [48] $y = c(x) = \sum_i a_i x^i$, $i = 1, 2, \dots, 5$, with coefficients $a_1 = 1.22bh/L$, $a_2 = 3.19bh/L^2$, $a_3 = -15.73bh/L^3$, $a_4 = 21.87bh/L^4$ and $a_5 = -10.55bh/L^5$, where $bh = 0.4$ represents the maximum body thickness and $L = 3.738$ denotes the body length. No-slip boundary condition is imposed on the top and bottom walls, while inflow and outflow conditions are applied at the left and right sides of the domain, respectively. The inflow is realized by a velocity profile of $U(y) = 1.5\bar{U}(t)y(H-y)/H^2$ with a start-up smooth procedure $\bar{U}(t) = 0.5(1.0 - \cos(0.5\pi t))$ if $t \leq 4.0$ otherwise $\bar{U}(t) = 1.0$. The fluid density $\rho^F = 1.0$ and the Reynolds number $Re = \frac{U_0 L}{\eta} = 5000$. The Neo-Hookean material model is used for the body with dimensionless Young's modulus $E^* = E/\rho^F U_0^2 = 200$, Poisson's ratio $\nu = 0.49$ and density $\rho^S = \rho^F$. To discretize the system, the initial particle spacing of the body is about $dp^S = bh/8.0$ and the resolution ratio $dp^F/dp^S = 2.0$. Note that a rigid body constraint is applied to the head of the body.

Fig. 17 depicts snapshots of the flow field colored by the vorticity and the body colored by von Mises stress. The four frames approximately span a flapping period. As the flapping has reached a sustained stage, a trail of vorticity forms in the wake behind the body. Vortices with opposite signs are shed alternately from the tail at the moment when the body is most bent. This flow pattern is in agreement with the experimental results of Zhang et al. [49], which showed that a trail of vortices is produced by flexible filaments in a flowing soap film.

In Fig. 18, the x and y positions of the head and tail are plotted as functions of time. It is observed that the sustained flapping is achieved at about non-dimensional time $t = 50$, after the fish has adjusted its position from the middle to upper region. The fish-like body shows slow oscillating migrations near the mean location at about $y \approx 5.0$. Numerical experiments (not shown here) show the body may achieve sustained flapping in the lower region if a slightly different initial particle distribution is used for the body. Such migration behaviors may be related to the fact that the flow speed is reduced towards the walls and the upper or lower regions are energetically more favorable. It is also noted that the preliminary flapping frequency of the tail is around $0.8s^{-1}$, and the approximated vertical amplitude of the tail is about 0.15, i.e. 4% of the size of the body width. Also note that the flexible body undergoes a traveling wave motion as shown in Fig. 19, which is similar to the typical flapping pattern of an active fish swimming.

5. Concluding remarks

In this paper, we have presented a simple, efficient and accurate multi-resolution SPH method for fluid-structure interactions. The present method is capable of incorporating different spatial-temporal resolutions for the fluid and structure, and demonstrates a considerably improved computational efficiency. A position-based Verlet scheme is introduced to ensure the momentum conservation in fluid-structure coupling when multiple time steps are applied. Furthermore, the time-averaged velocity and acceleration of solid particles are introduced to enhance the force matching in fluid-structure coupling. Extensive numerical examples demonstrate the robustness and reasonable accuracy in reproducing the solid dynamics when a

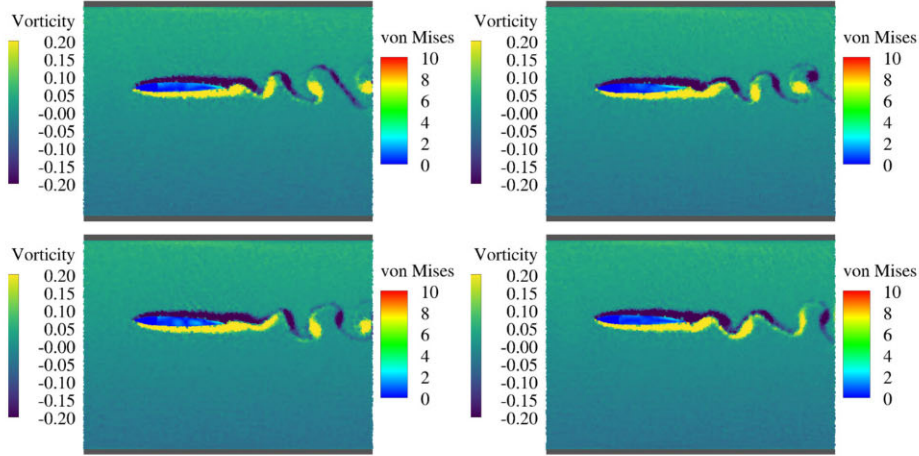


Fig. 17. Passive flapping of a flexible fish-like body: distributions of the von Mises stress in the body and vorticity in the flow at various time instants.

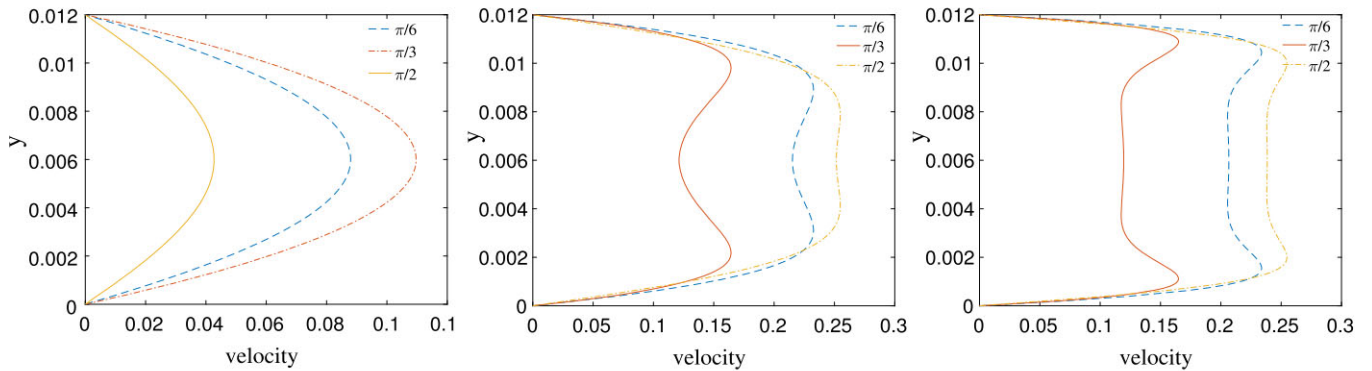


Fig. 18. Time histories of the head and tail positions of the flexible fish-like body: (a) head position in x -direction, (b) head position in y -direction, (c) tail position in x -direction, (d) tail position in y -direction, and (e) zoom-in view of the area A marked in (d).

coarser resolution is sufficient for the fluid dynamics. Special attention is paid to test the present method for applications in bio-mechanical systems, e.g. venous valve and passive flapping of a fish-like body. Though the model used here is quite simple, the obtained numerical results show promising potential to future more practical applications. Note that, in some applications the fluid computation may need higher spatial-temporal resolution than that of solid structure, for example when capturing near wall flow structure is of interest or considering highly viscous non-Newton fluids. In this case, other acceleration methods for fluid discretization, e.g. the implicit method or GPU computing, may be applicable.

CRediT authorship contribution statement

Chi Zhang: Investigation, Writing – original draft. **Massoud Rezavand:** Investigation. **Xiangyu Hu:** Conceptualization, Supervision.

Declaration of competing interest

The authors declare that they have no known competing financial interests or personal relationships that could have appeared to influence the work reported in this paper.

Acknowledgements

The authors would like to express their gratitude to Deutsche Forschungsgemeinschaft for their sponsorship of this research under grant number DFG HU1572/10-1 and DFG HU1527/12-1.

Appendix A. Velocity profile of the pulsative flow

Considering that the pulsative flow is driven by a periodic pressure gradient

$$\frac{\partial p}{\partial x} = -A \cos\left(\frac{2\pi}{T} t\right),$$

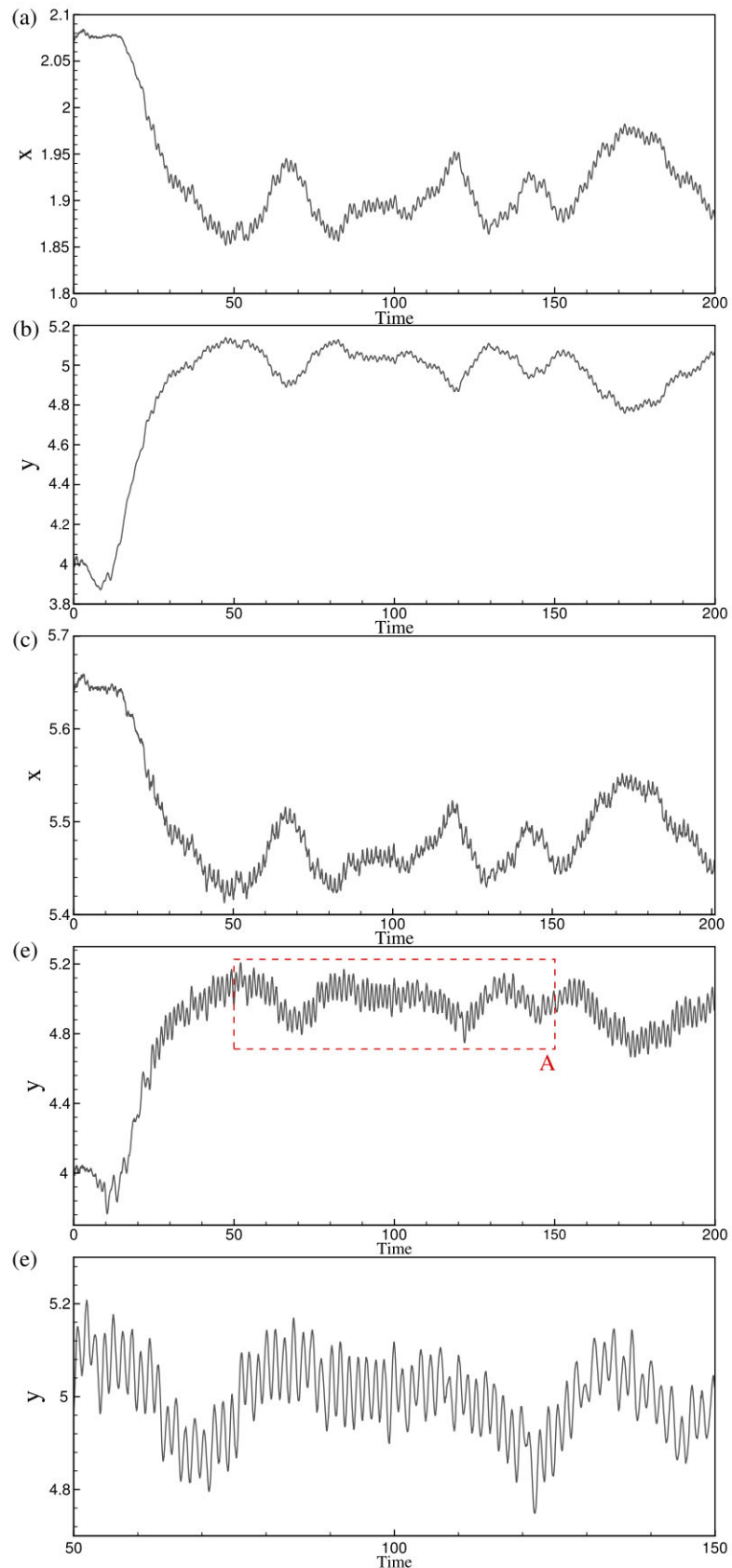


Fig. 19. Flapping pattern of the flexible fish-like body. Particles located at the central line of the body for a typical period of flapping.

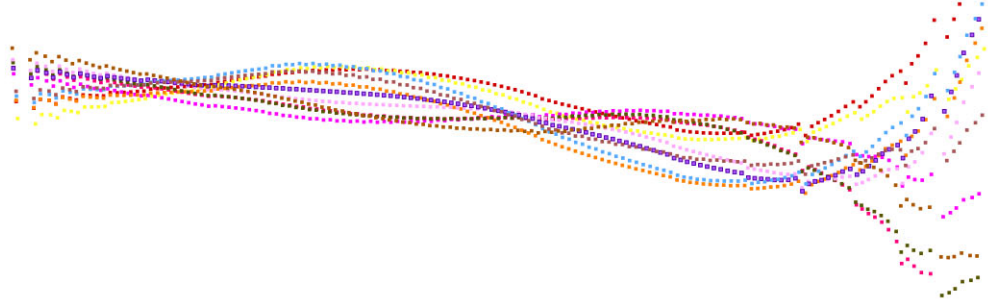


Fig. 20. Velocity profiles corresponding to the computational setup used in Section 4.4 during a typical period: $W_o = 1.0$ (left panel), $W_o = 5.0$ (middle panel) and $W_o = 10.0$ (right panel).

where A denotes the pressure amplitude and T the oscillation period. To mimic the pulsative flow in the model of Left Ventricle, we set $A_0 = 2500 N/m^3$ and $T_0 = 0.6 s$. The analytical solution for this type of flow is [50]

$$u_0(y, t) = \frac{A}{\omega \rho_f \gamma} \left\{ \left(\sinh(\Phi_1(y)) \sin(\Phi_2(y)) + \sinh(\Phi_2(y)) \sin(\Phi_1(y)) \right) \cos(\omega t) \right. \\ \left. \left(\gamma - \cosh(\Phi_1(y)) \cos(\Phi_2(y)) - \cosh(\Phi_2(y)) \cos(\Phi_1(y)) \right) \cos(\omega t) \right\},$$

where

$$\begin{cases} \Phi_1(y) = \frac{W_o}{\sqrt{2}} \left(1 + 2.0 \frac{y - \frac{1}{2} DH}{DH} \right) \\ \Phi_2(y) = \frac{W_o}{\sqrt{2}} \left(1 - 2.0 \frac{y - \frac{1}{2} DH}{DH} \right) \end{cases},$$

and

$$\gamma = \cosh(\sqrt{2} W_o) + \cos(\sqrt{2} W_o),$$

where W_o is the Womersley number. Fig. 20 gives velocity profiles of different W_o numbers.

References

- [1] T.E. Tezduyar, M. Behr, S. Mittal, J. Liou, A new strategy for finite element computations involving moving boundaries and interfaces, *Comput. Methods Appl. Mech. Eng.* 94 (3) (1992) 353–371.
- [2] C.S. Peskin, The immersed boundary method, *Acta Numer.* 11 (2002) 479–517.
- [3] E. Oñate, S. Idelsohn, O. Zienkiewicz, R. Taylor, A finite point method in computational mechanics. applications to convective transport and fluid flow, *Int. J. Numer. Methods Biomed. Eng.* 39 (22) (1996) 3839–3866.
- [4] L.B. Lucy, A numerical approach to the testing of the fission hypothesis, *Astron. J.* 82 (1977) 1013–1024.
- [5] R.A. Gingold, J.J. Monaghan, Smoothed particle hydrodynamics: theory and application to non-spherical stars, *Mon. Not. R. Astron. Soc.* 181 (3) (1977) 375–389.
- [6] C. Zhang, X. Hu, N.A. Adams, A weakly compressible SPH method based on a low-dissipation Riemann solver, *J. Comput. Phys.* 335 (2017) 605–620.
- [7] S. Koshizuka, Y. Oka, Moving-particle semi-implicit method for fragmentation of incompressible fluid, *Nucl. Sci. Eng.* 123 (3) (1996) 421–434.
- [8] B. Mishra, R.K. Rajamani, The discrete element method for the simulation of ball mills, *Appl. Math. Model.* 16 (11) (1992) 598–604.
- [9] C. Zhang, X.Y. Hu, N.A. Adams, A generalized transport-velocity formulation for smoothed particle hydrodynamics, *J. Comput. Phys.* 337 (2017) 216–232.
- [10] M. Rezavand, C. Zhang, X. Hu, A weakly compressible SPH method for violent multi-phase flows with high density ratio, *J. Comput. Phys.* 402 (2020) 109092.
- [11] C. Zhang, G. Xiang, B. Wang, X. Hu, N. Adams, A weakly compressible SPH method with WENO reconstruction, *J. Comput. Phys.* 392 (2019) 1–18.
- [12] C. Antoci, M. Gallati, S. Sibilla, Numerical simulation of fluid–structure interaction by SPH, *Comput. Struct.* 85 (11–14) (2007) 879–890.
- [13] G. Oger, P.M. Guilcher, E. Jacquin, L. Brosset, J.B. Deuff, D. Le Touzé, et al., Simulations of hydro-elastic impacts using a parallel SPH model, in: The Nineteenth International Offshore and Polar Engineering Conference, International Society of Offshore and Polar Engineers, 2009.
- [14] M. Liu, J. Shao, H. Li, Numerical simulation of hydro-elastic problems with smoothed particle hydrodynamics method, *J. Hydodyn.* 25 (5) (2013) 673–682.
- [15] L. Wang, F. Xu, Y. Yang, SPH scheme for simulating the water entry of an elastomer, *Ocean Eng.* 178 (2019) 233–245.
- [16] L. Zhan, C. Peng, B. Zhang, W. Wu, A stabilized TL-WC SPH approach with GPU acceleration for three-dimensional fluid–structure interaction, *J. Fluids Struct.* 86 (2019) 329–353.
- [17] L. Han, X. Hu, SPH modeling of fluid–structure interaction, *J. Hydodyn.* 30 (1) (2018) 62–69.
- [18] M. Liu, Z. Zhang, Smoothed particle hydrodynamics (SPH) for modeling fluid–structure interactions, *Sci. China, Phys. Mech. Astron.* 62 (8) (2019) 984701.
- [19] Z. Zhang, T. Long, J. Chang, M. Liu, A smoothed particle element method (SPEM) for modeling fluid–structure interaction problems with large fluid deformations, *Comput. Methods Appl. Mech. Eng.* 356 (2019) 261–293.
- [20] A. Rafiee, K.P. Thiagarajan, An SPH projection method for simulating fluid–hypoelastic structure interaction, *Comput. Methods Appl. Mech. Eng.* 198 (33–36) (2009) 2785–2795.
- [21] A. Khayyer, H. Gotoh, H. Falahaty, Y. Shimizu, An enhanced ISPH–SPH coupled method for simulation of incompressible fluid–elastic structure interactions, *Comput. Phys. Commun.* 232 (2018) 139–164.

- [22] P. Sun, D. Le Touzé, A.-M. Zhang, Study of a complex fluid-structure dam-breaking benchmark problem using a multi-phase SPH method with APR, *Eng. Anal. Bound. Elem.* 104 (2019) 240–258.
- [23] A. Khayyer, N. Tsuruta, Y. Shimizu, H. Gotoh, Multi-resolution MPS for incompressible fluid-elastic structure interactions in ocean engineering, *Appl. Ocean Res.* 82 (2019) 397–414.
- [24] B. Ren, Z. Jin, R. Gao, Y. Wang, Z. Xu, Sph-dem modeling of the hydraulic stability of 2d blocks on a slope, *J. Waterw. Port Coast. Ocean Eng.* 140 (6) (2013) 04014022.
- [25] Q. Yang, V. Jones, L. McCue, Free-surface flow interactions with deformable structures using an SPH-FEM model, *Ocean Eng.* 55 (2012) 136–147.
- [26] Y. Zhang, D. Wan, MPS-FEM coupled method for fluid-structure interaction in 3d dam-break flows, *Int. J. Comput. Methods* 16 (02) (2019) 1846009.
- [27] X. Chen, Y. Zhang, D. Wan, Numerical study of 3-d liquid sloshing in an elastic tank by MPS-FEM coupled method, *J. Ship Res.* (2019).
- [28] J.M. Owen, J.V. Villumsen, P.R. Shapiro, H. Martel, Adaptive smoothed particle hydrodynamics: Methodology. II, *Astrophys. J. Suppl. Ser.* 116 (2) (1998) 155.
- [29] D.A. Barcarolo, D. Le Touzé, G. Oger, F. De Vuyst, Adaptive particle refinement and derefinement applied to the smoothed particle hydrodynamics method, *J. Comput. Phys.* 273 (2014) 640–657.
- [30] M. Lastiwka, N. Quinlan, M. Basa, Adaptive particle distribution for smoothed particle hydrodynamics, *Int. J. Numer. Methods Fluids* 47 (10–11) (2005) 1403–1409.
- [31] R. Vacondio, B. Rogers, P. Stansby, P. Mignosa, J. Feldman, Variable resolution for SPH: a dynamic particle coalescing and splitting scheme, *Comput. Methods Appl. Mech. Eng.* 256 (2013) 132–148.
- [32] W. Hu, G. Guo, X. Hu, D. Negruț, Z. Xu, W. Pan, A consistent spatially adaptive smoothed particle hydrodynamics method for fluid–structure interactions, *Comput. Methods Appl. Mech. Eng.* 347 (2019) 402–424.
- [33] P. Omidvar, P.K. Stansby, B.D. Rogers, Wave body interaction in 2d using smoothed particle hydrodynamics (SPH) with variable particle mass, *Int. J. Numer. Methods Fluids* 68 (6) (2012) 686–705.
- [34] X. Bian, Z. Li, G.E. Karniadakis, Multi-resolution flow simulations by smoothed particle hydrodynamics via domain decomposition, *J. Comput. Phys.* 297 (2015) 132–155.
- [35] C. Zhang, M. Rezavand, Y. Zhu, Y. Yu, D. Wu, W. Zhang, S. Zhang, J. Wang, X. Hu, SPHinXsys: An open-source meshless, multi-resolution and multi-physics library, *Softw. Impacts* (2020) 100033.
- [36] J.J. Monaghan, Simulating free surface flows with SPH, *J. Comput. Phys.* 110 (2) (1994) 399–406.
- [37] J.P. Morris, P.J. Fox, Y. Zhu, Modeling low Reynolds number incompressible flows using SPH, *J. Comput. Phys.* 136 (1) (1997) 214–226.
- [38] R.W. Ogden, Non-linear elastic deformations, Courier Corporation, 1997.
- [39] R. Vignjevic, J.R. Reveles, J. Campbell, SPH in a total Lagrangian formalism, *CMC-Tech Science Press* 4 (3) (2006) 181.
- [40] S. Adami, X. Hu, N.A. Adams, A generalized wall boundary condition for smoothed particle hydrodynamics, *J. Comput. Phys.* 231 (21) (2012) 7057–7075.
- [41] C. Zhang, M. Rezavand, X. Hu, Dual-criteria time stepping for weakly compressible smoothed particle hydrodynamics, *J. Comput. Phys.* 404 (2020) 109135.
- [42] G. Fourey, C. Hermange, D. Le Touzé, G. Oger, An efficient FSI coupling strategy between smoothed particle hydrodynamics and finite element methods, *Comput. Phys. Commun.* 217 (2017) 66–81.
- [43] S. Turek, J. Hron, Proposal for numerical benchmarking of fluid-structure interaction between an elastic object and laminar incompressible flow, in: *Fluid-structure Interaction*, Springer, 2006, pp. 371–385.
- [44] R. Bhardwaj, R. Mittal, Benchmarking a coupled immersed-boundary-finite-element solver for large-scale flow-induced deformation, *AIAA J.* 50 (7) (2012) 1638–1642.
- [45] F. Tian, H. Dai, H. Luo, J.F. Doyle, B. Rousseau, Fluid–structure interaction involving large deformations: 3d simulations and applications to biological systems, *J. Comput. Phys.* 258 (2014) 451–469.
- [46] K. van Langevelde, A. Šrámek, F.R. Rosendaal, The effect of aging on venous valves, *Arterioscler. Thromb. Vasc. Biol.* 30 (10) (2010) 2075–2080.
- [47] W. Huang, S.J. Shin, H.J. Sung, Simulation of flexible filaments in a uniform flow by the immersed boundary method, *J. Comput. Phys.* 226 (2) (2007) 2206–2228.
- [48] M. Curatolo, L. Teresi, Modeling and simulation of fish swimming with active muscles, *J. Theor. Biol.* 409 (2016) 18–26.
- [49] J. Zhang, S. Childress, A. Libchaber, M. Shelley, Flexible filaments in a flowing soap film as a model for one-dimensional flags in a two-dimensional wind, *Nature* 408 (6814) (2000) 835.
- [50] C. Loudon, A. Tordesillas, The use of the dimensionless womersley number to characterize the unsteady nature of internal flow, *J. Theor. Biol.* 191 (1) (1998) 63–78.